

AN OPEN-SOURCE, AUTOMATED CHEMICAL VAPOR DEPOSITION SYSTEM
FOR THE PRODUCTION OF 2D MATERIALS

by

Dale Brown

A thesis

submitted in partial fulfillment

of the requirements for the degree of

Master of Science in Materials Science and Engineering

Boise State University

December 2015

© 2015

Dale Brown

ALL RIGHTS RESERVED

BOISE STATE UNIVERSITY GRADUATE COLLEGE

DEFENSE COMMITTEE AND FINAL READING APPROVALS

of the thesis submitted by

Dale Brown

Thesis Title: An Open-Source, Automated Chemical Vapor Deposition System for the
Production of 2D Materials

Date of Final Oral Examination: 19 October 2015

The following individuals read and discussed the thesis submitted by student Dale Brown, and they evaluated her presentation and response to questions during the final oral examination. They found that the student passed the final oral examination.

David Estrada, Ph.D.	Chair, Supervisory Committee
Kurtis Cantley, Ph.D.	Member, Supervisory Committee
Ashkan Behnam, Ph.D.	Member, Supervisory Committee
Elton Graugnard, Ph.D.	Member, Supervisory Committee

The final reading approval of the thesis was granted by David Estrada, Ph.D., Chair of the Supervisory Committee. The thesis was approved for the Graduate College by John R. Pelton, Ph.D., Dean of the Graduate College.

ACKNOWLEDGEMENTS

First of all, I would like to thank my advisor, Dr. David Estrada, for his guidance and support during my time at Boise State. I would like to thank my Integrated Nanomaterials Lab colleagues Nikki Chang, Richard Livingston, Benjamin Knipfer, and Kari McLaughlin for their help with the construction of the CVD, growth of materials, and analysis of materials. I would like to thank Dr. Elton Graugnard for his advice, for allowing me to see the parts list for his ALD system, and for serving on my thesis committee. Thank you to Dr. Kurtis Cantley in the Electrical Engineering department and Dr. Ashkan Behnam from Intel for serving on my thesis committee. Thanks to Dick Sevier for designing and constructing the CVD's power supply and to Dr. Yanliang Zhang for partial support during this project

This project was also supported by graduate fellowships from the Nuclear Research Council and NASA Idaho Space Grant. Additional funding was provided by faculty startup funds, generously provided by the Micron Foundation.

ABSTRACT

While interest in two-dimensional materials has exploded in recent years, the high cost of chemical vapor deposition (CVD) systems can act as a barrier to entry for some researchers interested in studying these materials. This thesis presents an open-source design for an automated CVD that can be built for a fraction of the cost of similarly capable commercial systems and that can easily be customized and expanded. With a CVD built as described, growth of high quality graphene and graphene foam is demonstrated. These results highlight the flexibility of the open-source design in producing a variety of nanomaterials, which are at the forefront of research in emerging semiconductor devices, bionanotechnology, and energy storage and conversion.

TABLE OF CONTENTS

ACKNOWLEDGEMENTS.....	iv
ABSTRACT.....	v
LIST OF FIGURES.....	ix
CHAPTER ONE: INTRODUCTION.....	1
1.1 Open-Source Technology.....	1
1.1.1 Free and Open-Source Software.....	2
1.1.2 Open-Source Hardware.....	3
1.2 Two-Dimensional Materials.....	6
1.2.1 Graphene – A Semi-Metallic 2D Material.....	6
1.2.2 Hexagonal Boron Nitride – A Dielectric 2D Material.....	7
1.2.3 Molybdenum Disulfide – A Semiconducting 2D Material.....	8
1.2.4 Other 2D Materials.....	9
1.2.5 2D Material Synthesis.....	9
1.2.6 2D Heterostructures.....	11
1.3 References.....	11
CHAPTER TWO: BACKGROUND INFORMATION.....	14
2.1 Current CVD Options.....	14
2.1.1 Build or Purchase a Manual CVD.....	14
2.1.2 Build an Automated CVD.....	14

2.1.3 Purchase an Automated CVD.....	15
2.2 A Fourth Option.....	16
2.3 Parameter Space of CVD Graphene Growth from Methane.....	17
2.4 References.....	19
CHAPTER THREE: EXPERIMENTAL METHODS – SYSTEM DESIGN.....	20
3.1 Hardware Design.....	21
3.1.1 Gas Delivery Lines.....	21
3.1.2 Gas Filter Lines.....	23
3.1.3 Mass Flow Controllers.....	23
3.1.4 Gas Mixing Line.....	24
3.1.5 Intake Manifold.....	25
3.1.6 Pressure Gauges.....	26
3.1.7 Reaction Tube.....	27
3.1.8 Furnace.....	28
3.1.9 Exhaust Manifold.....	29
3.1.10 Overpressure Relief.....	30
3.1.11 Vent Valve.....	31
3.1.12 Exhaust Line.....	32
3.1.13 Butterfly Valve.....	33
3.1.14 Vacuum Pump.....	34
3.1.15 Snorkel Manifold.....	35
3.1.16 Cables.....	36
3.1.17 Data Acquisition and Control.....	37
3.1.18 Base and Supports.....	38

3.2 Driver and Software Design.....	40
3.2.1 Device Drivers.....	40
3.2.2 Manual Control Program.....	40
3.2.3 Automatic Control Program.....	42
3.2.4 Auditability.....	47
CHAPTER FOUR: RESULTS AND DISCUSSION.....	50
4.1 Graphene.....	50
4.1.1 Graphene Growth.....	50
4.1.2 Graphene Characterization.....	51
4.2 Graphene Foam.....	54
4.1.2 Graphene Foam Growth.....	54
4.2.2 Graphene Foam Characterization.....	54
4.3 References.....	56
CHAPTER FIVE: CONCLUSION.....	58
5.1 Summary and Discussion.....	58
5.2 Future Work.....	59
5.3 References.....	59
CHAPTER SIX: SUPPLEMENTARY INFORMATION.....	60
6.1 Supplementary Materials Folder Description.....	60

LIST OF FIGURES

Figure 1.1	Open-source syringe pump with 3D-printed parts. Reproduced under terms of the Creative Commons Attribution License from [7].....	3
Figure 1.2	Open-source lab jack with 3D-printed parts. Reproduced under terms of the Creative Commons Attribution License from [8].....	4
Figure 1.3	Model of an open source scanning two-photon microscope. Reproduced under terms of the Creative Commons Attribution License from [9]....	5
Figure 1.4	Molecular model of a single-layer graphene crystal. The crystal consists of carbon atoms which are sp^3 bonded into a 2D sheet.....	6
Figure 1.5	Single-layer hexagonal boron nitride crystal structure. The structure is flat and similar to the graphene structure but half of the carbon atoms are replaced by nitrogen and the other half by boron.....	7
Figure 1.6	Single-layer crystal of molybdenum disulfide (MoS_2). In the case of MoS_2 , a single-layer crystal consists of three layers of atoms: a layer of molybdenum atoms (blue) sandwiched between two vertically-aligned layers of sulfur atoms (green, only upper layer shown). Adapted under terms of the Creative Commons Attribution License from [12].....	8
Figure 3.1	Front view of the final CVD hardware.....	20
Figure 3.2	Gas delivery line. Views show a) the inside of the gas cabinet and b) on the back side of the gas cabinet.....	22
Figure 3.3	Gas filter lines. MFCs are shown at the right.....	23
Figure 3.4	Gas mixing line.....	24
Figure 3.5	Intake manifold.....	25
Figure 3.6	Pressure gauges.....	26
Figure 3.7	Reaction tube assembly. Coloration downstream of the furnace center is mainly due to copper deposition from graphene growths.....	27
Figure 3.8	Tube furnace.....	28
Figure 3.9	Exhaust manifold.....	29
Figure 3.10	Overpressure relief line. a) Connection to top of exhaust manifold. b) Connection to room's exhaust snorkel.....	30
Figure 3.11	Vent valve assembly.....	31

Figure 3.12	Exhaust line. a) shows how the exhaust line is coupled to the exhaust manifold via a KF40 to KF25 adapter (part 1). b) shows the ball valve (part 7) and filter (part 10), while c) shows where the butterfly valve is integrated into the exhaust line.....	32
Figure 3.13	Butterfly valve.....	33
Figure 3.14	Vacuum pump subsystem.....	34
Figure 3.15	Snorkel manifold.....	35
Figure 3.16	System overview showing cable management.....	36
Figure 3.17	National Instruments cDAQ system with 2 modules. Note: An additional analog output module (part 3b) was added to the final design but not to our system.....	37
Figure 3.18	Base plate and support structures. a) Base plate in a system side view. b) Details of a manual valve support structure in the gas mixing line. c) Close up of a support for the molecular sieve filter. d) One of two securing brackets for the furnace.....	39
Figure 3.19	Screen capture of the ManualControls.vi control interface. Using this VI the pressure or valve state, gas flow rates, and furnace temperature can all be set and monitored.....	41
Figure 3.20	Contents of the Quick.csv recipe.....	42
Figure 3.21	Screen capture of the 'Check Recipe' tab of Read&RunRecipe.vi. When the VI is run and a recipe selected, the recipe will be checked and simulated, with the simulated growth profiles appearing in the graphs, plotted by both stage number and estimated growth time. If the growth profiles are acceptable as shown, the user can click 'Run Recipe' to begin the CVD system check.....	44
Figure 3.22	The 'System Check' tab of Read&RunRecipe.vi. When a CVD run has been started, the program will first conduct a system check to ensure that the furnace and butterfly valve are responding, the gases required for the recipe are available, the vacuum pump is on, and the CVD is sealed. If the system check succeeds, the user will be prompted for an experiment note then the recipe will start. If the system check fails, the CVD will be refilled with argon to room pressure and the program will end.....	45
Figure 3.23	The 'Run Recipe' tab of Read&RunRecipe.vi. After the system check has been passed and an experiment note entered, the state of the run can be monitored on this tab. The system state shown is 1 minute after the recipe switched from stage 1 to stage 2. The pressure dropped from ~500 Torr to ~300 Torr, the argon flow rate dropped from ~600 sccm to 0 sccm, the methane flow rate increased from 0 to ~400 sccm, and the furnace temperature setpoint is ramping to 500°C at 30°C/min.....	46

Figure 3.24	Plots resulting from running the Excel macro on the log file resulting from running the 'Quick.csv' recipe. Shown are a) the furnace temperature and setpoint, b) the pressure and setpoint, c) the gas flow rates, and d) the gas flow setpoints.....	48
Figure 3.25	CVD run logs for a Quick.csv recipe run during which the furnace was prematurely opened and the methane valve was turned off during the run.....	49
Figure 4.1	Recipe used for the growth of graphene on copper foil.....	50
Figure 4.2	Raman of graphene grown in the CVD system described. Trials were taken at 4 different places on the sample. Characteristic peaks at $\sim 1350\text{ cm}^{-1}$, $\sim 1585\text{ cm}^{-1}$, and $\sim 2685\text{ cm}^{-1}$ correspond to the D band, G band, and 2D band, respectively.....	51
Figure 4.3	Raman maps of four samples grown using identical recipes. Intensity shown is the ratio of the 2D peak height to the G peak height.....	52
Figure 4.4	Map of the integrated intensity of the G peak to that of the D peak for the four graphene samples.....	53
Figure 4.5	Recipe used for the growth of graphene foam onto nickel foam substrate.....	54
Figure 4.6	Raman of graphene foam on nickel with the background signal subtracted. The defect-related graphene D peak at $\sim 1350\text{ cm}^{-1}$ is absent in these spectra.....	55
Figure 4.7	a) SEM images of graphene grown on a metal foam. b) Closeup of graphene grown on nickel foam. The apparent wrinkles on the right side of the image are thought to be a result of the metal having a larger coefficient of thermal expansion than graphene. c) Graphene foam after the nickel foam substrate has been etched. Scale bars are $500\text{ }\mu\text{m}$, $20\text{ }\mu\text{m}$, and $500\text{ }\mu\text{m}$, respectively.....	56

CHAPTER ONE: INTRODUCTION

1.1 Open-Source Technology

Open-source technology, broadly speaking, is the field of technological development in which the design of the final product is published and freely available for others to reuse or adapt to their own needs. This is in contrast to the standard commercial approach to technological development where designs and software are often patented or kept as trade secrets, giving the company a monopoly in the development and use of the technology in question [1].

When a new hardware or software solution is desired, there are two main costs associated with its development. The first is engineering cost, that is, the cost of designing and testing the product, while the second is the incremental cost associated with producing each individual unit once the design has been finalized. In the traditional commercial approach, the engineering cost of a product is spread over the volume of product sold. Partially because of this, low volume products such as scientific equipment are often much more expensive than high volume products such as automobiles and consumer electronics, even though the latter are generally more complex and have higher total engineering costs. In the case of low volume scientific equipment, a relatively low number of units are made so a greater portion of the total engineering cost must be absorbed into the price of each unit.

In light of this, one of the chief benefits of open-source technology for scientific

applications lies in the reduction of the engineering cost for the development of low volume products. An extreme example of this is the case in which a scientist needs a piece of custom equipment. They must either design and build the equipment themselves, paying the engineering cost with their own labor, or pay these costs to a company that does custom work. The time required for the first and the cost required for the second can put many experiments out of reach for a researcher with low funding. If, on the other hand, someone else in the field had previously published an open-source design for a piece of equipment similar to what was needed, the scientist could adapt the design to their needs, potentially reducing the engineering cost associated with building custom equipment by an order of magnitude or more, and a similar argument could be made for software.

The open-source technology field can be divided into two main sections: software and hardware, as discussed below.

1.1.1 Free and Open-Source Software

Free and open-source software (FOSS) has a long history and its popularity has been bolstered by its widespread adoption on the Internet, where consistent communication protocols are necessary and newcomers often benefit more from adopting the existing standards than they would from trying to create and promote their own standards [1]. In the scientific arena, Linux, an open-source operating system first released in 1991 by Linus Torvalds [2], has run on the majority of the top 500 supercomputers for over a decade [3], and as of June 2015 was the operating system on 488 of the top 500 supercomputers [4].

1.1.2 Open-Source Hardware

The history of open-source hardware is shorter and less storied. One of the most widely known examples of open-source hardware is Arduino, a group of electronic prototyping platforms with an accompanying open-source integrated development environment (IDE) [5]. While the Arduino board designs are open source, and many have created derivatives of them, much of the usefulness of the Arduino ecosystem lies in the code and design-sharing community that has risen around it. By using and modifying this shared code base, complex microcontroller solutions can be designed and built much faster than was possible without Arduino boards and the similar systems that have arisen around Arduino.

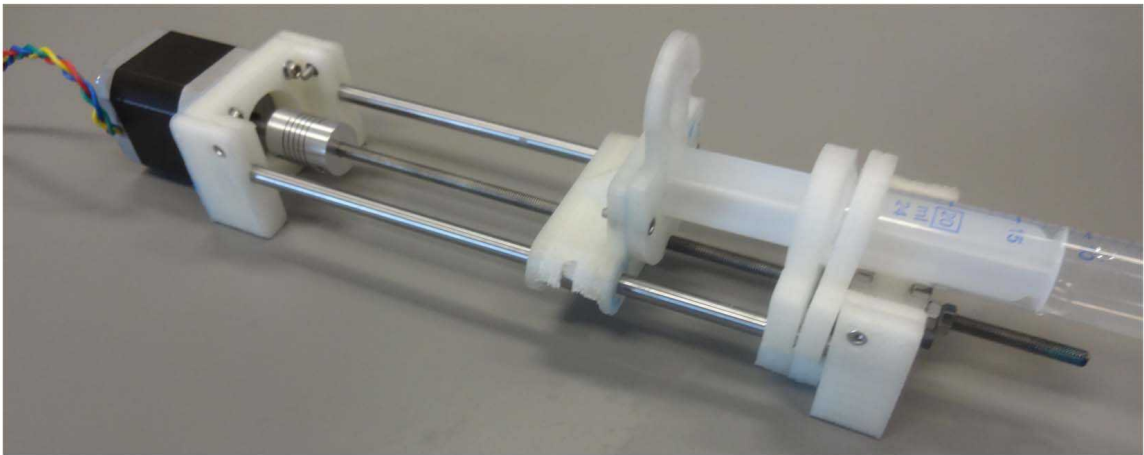


Figure 1.1 Open-source syringe pump with 3D-printed parts. Reproduced under terms of the Creative Commons Attribution License from [7].

Another notable open-source hardware that has been widely adopted is the RepRap open-source 3D printer [6]. With it, researchers have recently built open-source syringe pumps and optics equipment, both at an order or greater reduction in price from commercial equipment. And while much of the resulting equipment has reported

functionality equivalent to commercial products, those that don't can still lead to a large reduction in the cost of educational equipment, allowing for the outfitting of educational labs using a fraction of the budget needed for commercial equipment [7,8]. One variation of the syringe pump is shown in Figure 1.1, while one of the pieces of optical equipment, a lab jack, is shown in Figure 1.2.



Figure 1.2 Open-source lab jack with 3D-printed parts. Reproduced under terms of the Creative Commons Attribution License from [8].

On the other end of the spectrum, Rosenegger *et al.* recently demonstrated an open-source scanning two-photon microscope, shown in Figure 1.3, with a signal-to-noise ratio that exceeded those of the commercial systems they tested and represented savings in excess of \$150k. That magnitude of savings could bring research that requires a two-photon microscope into reach for many scientists for which funding is low, and the estimated two month build time for two inexperienced researchers is easily

within reach of many labs [9].

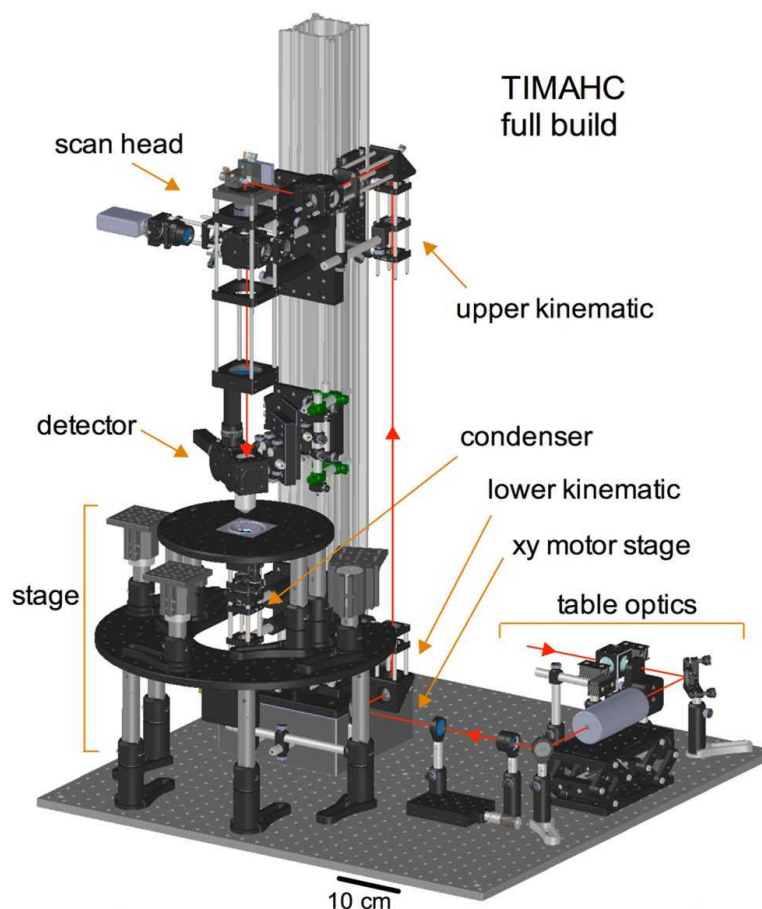


Figure 1.3 Model of an open-source scanning two-photon microscope. Reproduced under terms of the Creative Commons Attribution License from [9].

As open-source scientific hardware gains traction, it is perceivable that the rate of scientific discovery could increase as a result as researchers spend fewer resources acquiring commercial equipment or designing their own equipment and are freed to spend more time and effort conducting experiments. This work represents a small contribution to that idea in the form of an open-source chemical vapor deposition system for the production of two-dimensional materials.

1.2 Two-Dimensional Materials

1.2.1 Graphene – A Semi-Metallic 2D Material

The modern research push into two-dimensional (2D) materials was sparked by Novoselov and Geim's isolation of few- and single-layer graphene via the mechanical exfoliation of graphite, work originally published in 2004 [10]. The mechanical exfoliation was carried out by peeling layers of graphite off of a bulk crystal with tape and then repeating the process with the continually thinner graphite crystal left on the tape until single- or few-atom thick crystals are remaining. Novoselov et al. discovered that these single- and few-atom thick crystals of graphitic carbon, known as graphene, were stable in air, semi-metallic, and had extremely high mobilities (about $10,000 \text{ cm}^2 / \text{Vs}$), though the on/off ratio of graphene transistors was found to be less than 30 at room temperature, limiting its usefulness as the active component in transistors. The transport

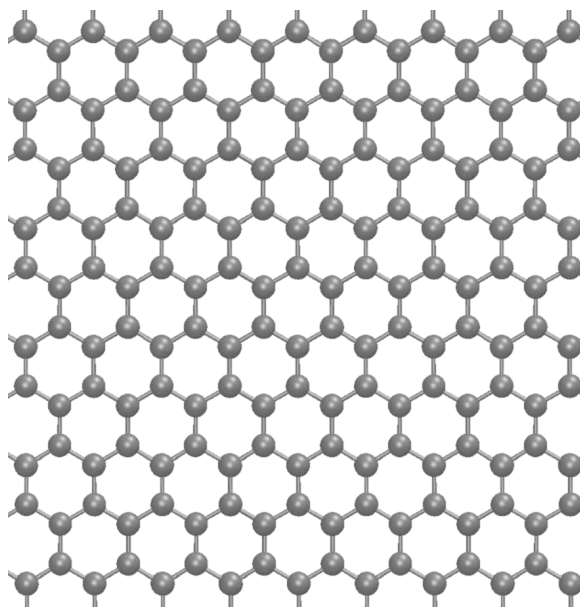


Figure 1.4 Molecular model of a single-layer graphene crystal. The crystal consists of carbon atoms that are sp^3 bonded into a 2D sheet.

of electrons was also found to be ballistic over distances up to 0.4 μm , evidence for the high quality of the resulting crystals [10]. Single-layer graphene is atomically flat, consisting of carbon atoms sp^3 bonded in a hexagonal array, as shown in Figure 1.4.

1.2.2 Hexagonal Boron Nitride – A Dielectric 2D Material

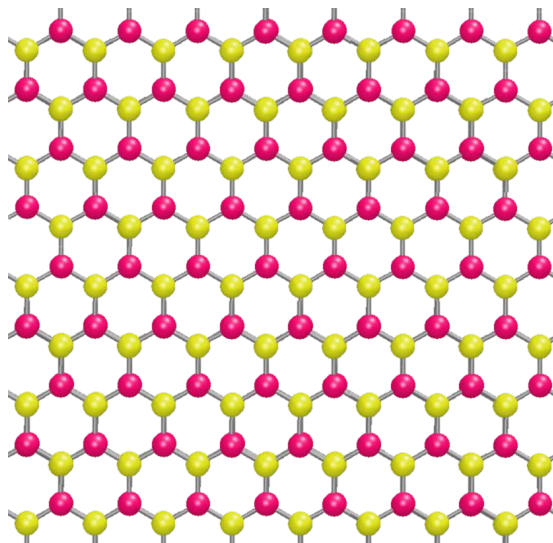


Figure 1.5 Single-layer hexagonal boron nitride crystal structure. The structure is flat and similar to the graphene structure but half of the carbon atoms are replaced by nitrogen and the other half by boron.

If the two carbon atoms in a graphene unit cell were replaced with nitrogen and boron, the resulting crystal is hexagonal boron nitride (hBN), as shown in Figure 1.5. Though similar to graphene in crystal structure and lattice constant (within 1.7%), while graphene has two bands that meet in a point at its Fermi level, making it a semimetal, hBN has a 5.97 eV bandgap, making it an insulator. Like graphene, hBN is also chemically inert and thought to be free of dangling bonds and other potential charge traps. The combination of these properties with its favorable dielectric properties make

hBN a potential replacement for the crystalline oxides currently used as substrates and dielectrics in 2D devices [11]. In one experiment, graphene was mechanically placed onto both hBN and SiO₂ substrates and the hBN sample showed order of magnitude improvements in both mobility and carrier inhomogeneity [11].

1.2.3 Molybdenum Disulfide – A Semiconducting 2D Material

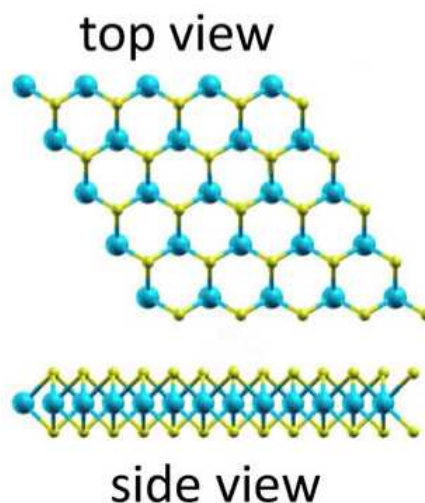


Figure 1.6 Single-layer crystal of molybdenum disulfide (MoS₂). In the case of MoS₂, a single-layer crystal consists of three layers of atoms: a layer of molybdenum atoms (blue) sandwiched between two vertically-aligned layers of sulfur atoms (green, only upper layer shown). Adapted under terms of the Creative Commons Attribution License from [12].

The third 2D material we will look at is molybdenum disulfide (MoS₂). While graphene and hBN are both one atom thick in single-layer crystals, a single layer of MoS₂ consists of three atomic layers: a layer of molybdenum surrounded by two aligned layers of sulfur, as shown in Figure 1.6 [12]. While bulk MoS₂ is an indirect-gap semiconductor, having a band gap of 1.29 eV, as the number of MoS₂ layers in a crystal

decreases, the indirect band gap increases, eventually reaching 1.90 eV in single layer crystals, making a ~ 1.8 eV direct gap the narrowest gap in the band structure. So, as the thickness of a MoS₂ crystal decreases, the band gap transitions from indirect in the bulk to direct in few- and single-layer crystals. One interesting result of this is a massive increase in the photoluminescence quantum yield of MoS₂ crystals as the thickness is decreased. While bulk crystals have a negligible quantum yield, quantum yields as high as 4×10^{-3} were observed on one study for monolayer crystals [13].

1.2.4 Other 2D Materials

While the 2D materials already discussed can be used as conductors, dielectrics, semiconductors, light emitters, and light detectors, there are a wealth of other 2D materials that have been studied. These include an analog of graphene that contains silicon instead of carbon; silicene, which is also a semimetal, chemically modified graphene where some of graphene's pi-bonds are broken and covalent bonds are made out of the plane, including fluorgraphene and graphene oxide, transition metal dichalcogenides besides MoS₂ including tungsten disulfide and tungsten and tungsten and molybdenum diselenide, other layered chalcogenides, layered oxides like micas, and others. There are many good reviews of 2D materials that provide additional details [14–17].

1.2.5 2D Material Synthesis

There are two general classes of 2D materials synthesis methods: top-down and bottom-up. In top-down synthesis methods, layers are removed from a large crystal of a layered material until only one or a few layers remain. One method, called mechanical exfoliation, accomplishes this using tape, as was done for the first isolation of

single-layer graphene [10]. Other top-down methods, generally referred to as exfoliation, include photoexfoliation, which uses laser energy to push layers apart, liquid exfoliation, which often uses high energy ultrasonic waves and the accompanying cavitation bubbles to separate layers [16], and lithium intercalation, where lithium ions infiltrate between layers of a material and then form bubbles on the introduction of water [18].

Though mechanical exfoliation yields high quality crystals, the method is limited by an inability to scale production to large volumes. Other exfoliation methods can produce higher yields of single- and few-layer flakes, but the resulting flakes are often small or damaged as a result of the exfoliation. For this reason, much research has been done in the bottom-up synthesis of 2D materials using a variety of approaches. These methods include molecular beam epitaxy (MBE), chemical synthesis, and chemical vapor deposition. While molecular beam epitaxy gives fine control over layer thickness of the deposited films [16], and it has been used to grow layered crystals with some of the lowest thermoconductivities thus far recorded [19], the high cost and low throughput associated with the method limit its appeal. Chemical synthesis of 2D materials, most often graphene, uses large flat, high-carbon precursors as building blocks for crystal layers. Much progress has been made in graphene synthesis, but broad use for the production of 2D materials is limited [16].

Chemical vapor deposition (CVD), a family of synthesis processes used widely in the production of commercial microelectronics, is one of the most studied methods for the production of 2D materials. Single crystals and films of single- and few-layer graphene, hBN, MoS₂, and other TMDs have all been grown via CVD. Graphene has been produced on both metal and insulating substrates [16], hBN has been grown directly

onto CVD-grown graphene [20], MoS₂ directly onto hBN [21], and a host of additional examples of the CVD growth of 2D materials can be found in the literature. This thesis details the design and construction of a CVD that is capable of conducting many of these growths.

1.2.6 2D Heterostructures

While 2D materials in isolation are an interesting and productive field of study, much of the promise of 2D materials is in the devices and materials that can be made when they are stacked and patterned. 2D materials that have been stacked with other 2D materials are often called two-dimensional heterostructures. These crystals are similar to bulk layered crystals, where the layers are held together with weak van der Waals forces, but layers are generally not the same type of crystal and their lattices are not aligned. While this thesis is concerned with the production of a chemical vapor deposition system for 2D materials synthesis, much of the promise of 2D materials is in the production of heterostructures and related reviews can be found in the literature [14,17,22,23].

1.3 References

1. Deek FP, McHugh JAM. Open Source: Technology and Policy. Cambridge University Press; 2007.
2. What Is Linux: An Overview of the Linux Operating System [Internet]. 2009 [cited 16 Sep 2015]. Available: <https://www.linux.com/learn/new-user-guides/376-linux-is-everywhere-an-overview-of-the-linux-operating-system>
3. Vaughan-Nichols SJ. Linux still owns supercomputing [Internet]. 2014 [cited 16 Sep 2015]. Available: <http://www.zdnet.com/article/linux-still-owns-supercomputing/>
4. Top500 The List [Internet]. 2015 [cited 16 Sep 2015]. Available: <http://www.top500.org/statistics/sublist/>
5. Arduino - Introduction [Internet]. [cited 16 Sep 2015]. Available: <https://www.arduino.cc/en/Guide/Introduction>
6. RepRap - RepRapWiki [Internet]. [cited 16 Sep 2015]. Available: <http://reprap.org/>

7. Wijnen B, Hunt EJ, Anzalone GC, Pearce JM. Open-Source Syringe Pump Library. *PLoS One*. 2014;9: e107216. doi:10.1371/journal.pone.0107216
8. Zhang C, Anzalone NC, Faria RP, Pearce JM. Open-Source 3D-Printable Optics Equipment. *PLoS One*. 2013;8. doi:10.1371/journal.pone.0059840
9. Rosenegger DG, Tran CHT, LeDue J, Zhou N, Gordon GR. A High Performance, Cost-Effective, Open-Source Microscope for Scanning Two-Photon Microscopy that Is Modular and Readily Adaptable. *PLoS One*. 2014;9: e110475. doi:10.1371/journal.pone.0110475
10. Novoselov KS, Geim AK, Morozov S V, Jiang D, Zhang Y, Dubonos S V, et al. Electric field effect in atomically thin carbon films. *Science*. 2004;306: 666–669. doi:10.1126/science.1102896
11. Dean CR, Young a F, Meric I, Lee C, Wang L, Sorgenfrei S, et al. Boron nitride substrates for high-quality graphene electronics. *Nat Nanotechnol*. 2010;5: 722–726. doi:10.1038/nnano.2010.172
12. Cong WT, Tang Z, Zhao XG, Chu JH. Enhanced Magnetic Anisotropies of Single Transition-Metal Adatoms on a Defective MoS₂ Monolayer. *Sci Rep*. 2015;5: 9361. doi:10.1038/srep09361
13. Mak KF, Lee C, Hone J, Shan J, Heinz TF. Atomically thin MoS₂: A new direct-gap semiconductor. *Phys Rev Lett*. 2010;105: 2–5. doi:10.1103/PhysRevLett.105.136805
14. Geim AK, Grigorieva I V. Van der Waals heterostructures. *Nature*. Nature Publishing Group; 2013;499: 419–25. doi:10.1038/nature12385
15. Koski K, Cui Y. The new skinny in two-dimensional nanomaterials. *ACS Nano*. 2013; 3739–3743. Available: <http://pubs.acs.org/doi/abs/10.1021/nn4022422>
16. Bonaccorso F, Lombardo A, Hasan T, Sun Z, Colombo L, Ferrari AC. Production and processing of graphene and 2d crystals. *Mater Today*. Elsevier Ltd; 2012;15: 564–589. doi:10.1016/S1369-7021(13)70014-2
17. Wang QH, Kalantar-Zadeh K, Kis A, Coleman JN, Strano MS. Electronics and optoelectronics of two-dimensional transition metal dichalcogenides. *Nat Nanotechnol*. Nature Publishing Group; 2012;7: 699–712. doi:10.1038/nnano.2012.193
18. Murphy DW, Salvo FJ, Hull GW, Waszczak J V. Convenient Preparation and Physical Properties of Lithium Intercalation Compounds of Group 4B and 5B Layered Transition Metal Dichalcogenides. *Inorg Chem*. 1976;15: 17–21. doi:10.1021/ic50155a005
19. Chiritescu C, Cahill D, Nguyen N. Ultralow thermal conductivity in disordered, layered WSe₂ crystals. *Science (80-)*. 2007;364: 2005–2007. Available: <http://www.sciencemag.org/content/315/5810/351.short>
20. Liu Z, Song L, Zhao S, Huang J, Ma L, Zhang J, et al. Direct growth of graphene/hexagonal boron nitride stacked layers. *Nano Lett*. 2011;11: 2032–2037.

doi:10.1021/nl200464j

21. Wang S, Wang X, Warner JH. All Chemical Vapor Deposition Growth of MoS₂:h-BN Vertical van der Waals Heterostructures. *ACS Nano*. 2015; 150420154824007. doi:10.1021/acsnano.5b00655
22. Fiori G, Bonaccorso F, Iannaccone G, Palacios T, Neumaier D, Seabaugh A, et al. Electronics based on two-dimensional materials. *Nat Nanotechnol*. 2014;9: 768–779. doi:10.1038/nnano.2014.207
23. Lin Y-C, Lu N, Perea-Lopez N, Li J, Lin Z, Peng X, et al. Direct synthesis of van der Waals solids. *ACS Nano*. 2014;8: 3715–23. doi:10.1021/nn5003858

CHAPTER TWO: BACKGROUND INFORMATION

2.1 Current CVD Options

If a researcher wants to enter the field of CVD-grown 2D materials, they have a few options: Build or purchase a manually controlled CVD, purchase an automated CVD, or build an automated CVD. In this section, we will consider the pros and cons of each option.

2.1.1 Build or Purchase a Manual CVD

The main advantage of a manually controlled CVD is its low cost relative to automated systems. A manual system that is otherwise nearly equivalent to the open-source CVD described herein can be purchased for about \$19,000 from MTI (personal communication, September 24, 2015), making it much more affordable than the automated systems described below. The chief disadvantage of this option is the high time requirement needed to operate a manual system. Additionally, for a manual system, all recipe execution and logging must be done by hand, making both consistency between growths and auditing of past growths depend highly on the skill and possibly fatigue level of the operator.

2.1.2 Build an Automated CVD

The next most expensive option is for the researcher to design, build, and program an automated CVD. This option is more inexpensive than purchasing an automated CVD, costing about \$30,000 for parts as compared with \$95,000 for a turn-key system (Y. Tu,

personal communication, August 31, 2015), but the engineering cost shows up in the time required for design, part acquisition, building, and programming of the system, the total duration of which depends heavily on the experience of the researchers conducting the build. And all the while, the researcher must be payed, giving the engineering cost of building a custom system an unknown monetary cost. Further, any time spent building a CVD system is time lost from the original goal of conducting research.

The benefits of an automated system above a manual system include a lower time investment requirement for each growth, increased repeatability if the control program allows for the use of recipes, and the ability to audit past growths if the controls record growth logs. Additional benefits include the possibility for a high level of customization, the ability to modify and update the system at a later date without having to void a system warranty to do so, and a significant gain of experience in vacuum systems and system automation for those conducting the build.

2.1.3 Purchase an Automated CVD

The third option is to purchase a turn-key system. The main advantage of this approach is that the researcher will be able to grow 2D materials while spending the least amount of time working on procuring a CVD with automation capabilities. They will also have many of the other benefits of having an automated CVD, depending on the specs of the device purchased, including a high level of consistency between growths with the use of recipes, a low time investment required for growths, and the ability to audit past growths by looking at growth logs.

The main disadvantage of purchasing an automated CVD is the high cost. Because CVD manufacturers generally have a low volume of sales, they must spread

their engineering costs over a small number of units, pushing up the price. According to recent quote requests, a CVD with capabilities on par with the open-source design described herein would cost anywhere from \$95,000 to \$170,000 (Y. Tu, personal communication, August 31, 2015; A. Kumar, personal communication, September 2, 2015), a cost that is three to six times that spent on parts for the design described herein. Other disadvantages include an inability to modify the closed-source controls programs, and a potential difficulty modifying the system hardware without voiding the warranty or losing support.

2.2 A Fourth Option

So as things stand, a researcher has to choose between purchasing a manually controlled system, saving money and time but not gaining the ability to automatically run recipes or audit past runs, designing, building, and programming an automated system, gaining the benefits of automation and a lower cost while losing both time and the cost of labor of those building the system, or they can purchase a turn-key system if they have the funds.

This thesis presents a fourth option: With the open-source design described herein, a researcher could build their own automated system without having to cover the entire engineering cost of designing and programming an automated system. This could bring down the barrier to entry into 2D materials research that acquiring an automated CVD represents, leading to an increased participation in 2D materials research and potentially to an acceleration in the development of nanoelectronics and other fields where 2D materials could be applied.

2.3 Parameter Space of CVD Graphene Growth from Methane

For this study, 2D graphene was grown on copper foil. Graphene has also been grown on nickel, ruthenium, and cobalt, but most of the research has focused onto nickel and copper foils. The high solubility of carbon in nickel and cobalt (> 0.1 atom %) leads to a high incidence of multilayer regions when the metal cools and the carbon atoms precipitate to the surface, making it difficult to consistently grow single- and few-layer graphene samples. Carbon has a low solubility in copper (<0.001 atom %), however, allowing for the growth of large area graphene films on copper foil and sputtered copper films [1]. In light of this, much of the research on large area graphene growth has shifted to the use of copper [2–4].

In one study, running a 35:2 ratio of methane to hydrogen at low pressures (LPCVD) and a temperature of 1000°C , graphene growths on copper foil that lasted 60 minutes were found to have similar graphene thicknesses to growths that lasted 10 minutes, being mostly mono-layer with a small area ($<5\%$) multi-layer. This suggests that graphene growth on copper foil from methane is self-limiting, leading to a higher consistency between growths, and that graphene growth from methane on copper is a surface-catalyzed process [2].

In another study, graphene was grown onto copper foil using a variety of methane to hydrogen ratios, and sometimes adding argon, at both atmospheric pressure and low pressure (625 mTorr). The atmospheric graphene growths were found to be non-uniform with large, multi-layer domains over a mono-layer base, suggesting that atmospheric growths of graphene on copper are not self-limiting as are low pressure growths. The researchers' conclusion for this difference is that the diffusion of methane to the sample's

surface is the rate-limiting step in the atmospheric pressure case. This means that uneven methane flux rates across the surface of the substrate lead to inconsistent graphene growth rates, resulting in uneven films. For the low pressure case, on the other hand, diffusion of methane is much faster as a result of larger mean free paths at lower pressures, and the reaction of methane with the surface is the rate limiting step. And because the rate limiting step is largely uniform over the surface of a sample in the LPCVD case, the resulting films are more uniform [1].

Temperatures for high quality graphene growth must be quite high. In one study, graphene was grown in an LPCVD at temperatures from 800°C to 1000°C, and the concentration of defects, as determined by the ratio of the intensity of the D Raman peak to the G Raman peak (I_D/I_G), decreased dramatically as the temperature increased. At 800°C, I_D/I_G was greater than 2, indicating a high concentration of defects, while at 1000°C the ratio was about 0.05, indicating low defect, high quality graphene. One factor that can be a problem with growing at this temperature, however, is the loss of copper from sublimation [5]. Evidence of this can be seen clearly in our CVD system in Figure 3.7.

The recipe used to demonstrate growth of graphene for this thesis (Figure 4.1) was adapted from [6] and uses methane, hydrogen, and argon, low pressures, a growth temperature of 1000°C, and a ratio of methane to hydrogen of 17. Based on the parameter spaces explored above, these growth conditions were expected to produce high quality films of mostly mono-layer graphene.

2.4 References

1. Bhaviripudi S, Jia X, Dresselhaus MS, Kong J. Role of kinetic factors in chemical vapor deposition synthesis of uniform large area graphene using copper catalyst. *Nano Lett.* 2010;10: 4128–33. doi:10.1021/nl102355e
2. Li X, Cai W, An J, Kim S, Nah J, Yang D, et al. Large-area synthesis of high-quality and uniform graphene films on copper foils. *Science.* 2009;324: 1312–4. doi:10.1126/science.1171245
3. Kim KS, Zhao Y, Jang H, Lee SY, Kim JM, Kim KS, et al. Large-scale pattern growth of graphene films for stretchable transparent electrodes. *Nature.* Nature Publishing Group; 2009;457: 706–710. doi:10.1038/nature07719
4. Reina A, Jia XT, Ho J, Nezich D, Son HB, Bulovic V, et al. Few-Layer Graphene Films on Arbitrary Substrates by Chemical Vapor Deposition. *Nano Lett.* 2009;9: 30–35. doi:10.1021/nl801827v
5. Kidambi PR, Ducati C, Dlubak B, Gardiner D, Weatherup RS, Martin MB, et al. The parameter space of graphene chemical vapor deposition on polycrystalline Cu. *J Phys Chem C.* 2012;116: 22492–22501. doi:10.1021/jp303597m
6. Banerjee S, Shim J, Rivera J, Jin X, Estrada D, Solovyeva V, et al. Electrochemistry at the edge of a single graphene layer in a nanopore. *ACS Nano.* 2013;7: 834–843. doi:10.1021/nm305400n

CHAPTER THREE: EXPERIMENTAL METHODS – SYSTEM DESIGN

Using variations of the design herein, a three gas, low pressure/atmospheric pressure CVD (Figure 3.1) could be built for around \$26k worth of parts, while a three gas, atmospheric pressure CVD could be built with around \$16k of parts, the latter being upgradeable to an LPCVD via the addition of the low pressure subsystems. Also, because the parts list (see supplementary material files) is divided by subsystem, a researcher or technician could easily swap out parts of a subsystem from the design, add or remove entire subsystems, or adapt subsystems and their LabView drivers for use in non-CVD applications.



Figure 3.1 Front view of the final CVD hardware.

The following sections describe the design's main subsystems, as detailed on the parts list. No claim is made that the design described is optimized. Rather, the design should be seen as a functional first attempt at an open-source CVD, and anyone using this design as a guide should verify that each subsystem including LabView drivers and control programs satisfies the specifications desired for their final system.

3.1 Hardware Design

See the supplementary materials for construction notes with higher resolution subsystem images annotated by part number and the parts list for component descriptions.

3.1.1 Gas Delivery Lines

The gas canisters for the system were placed into a gas cabinet immediately behind the table holding the CVD. With the use of flexible hoses (part 7 in Figure 3.2a), gas canisters can easily be removed via the disconnecting of the VCR fitting (parts 4 and 7) and the unthreading of the remaining $\frac{1}{4}$ solid section (parts 2-5). To reattach the gas line to a new canister, the steps above are done in reverse with new Teflon tape, while the VCR gasket (part 6) must be replaced before reattachment of the VCR fitting to ensure a proper seal.

Figure 3.2b shows the gas line routing from the back of the gas cabinet to the gas filter lines. The $\frac{1}{4}$ inch stainless tubing (part 10) was cut and bent by hand, with the bend in the middle allowing for a limited amount of play when connecting the downstream VCR fitting to the gas filter line. This subsystem would need to be modified for any other gas canister location.

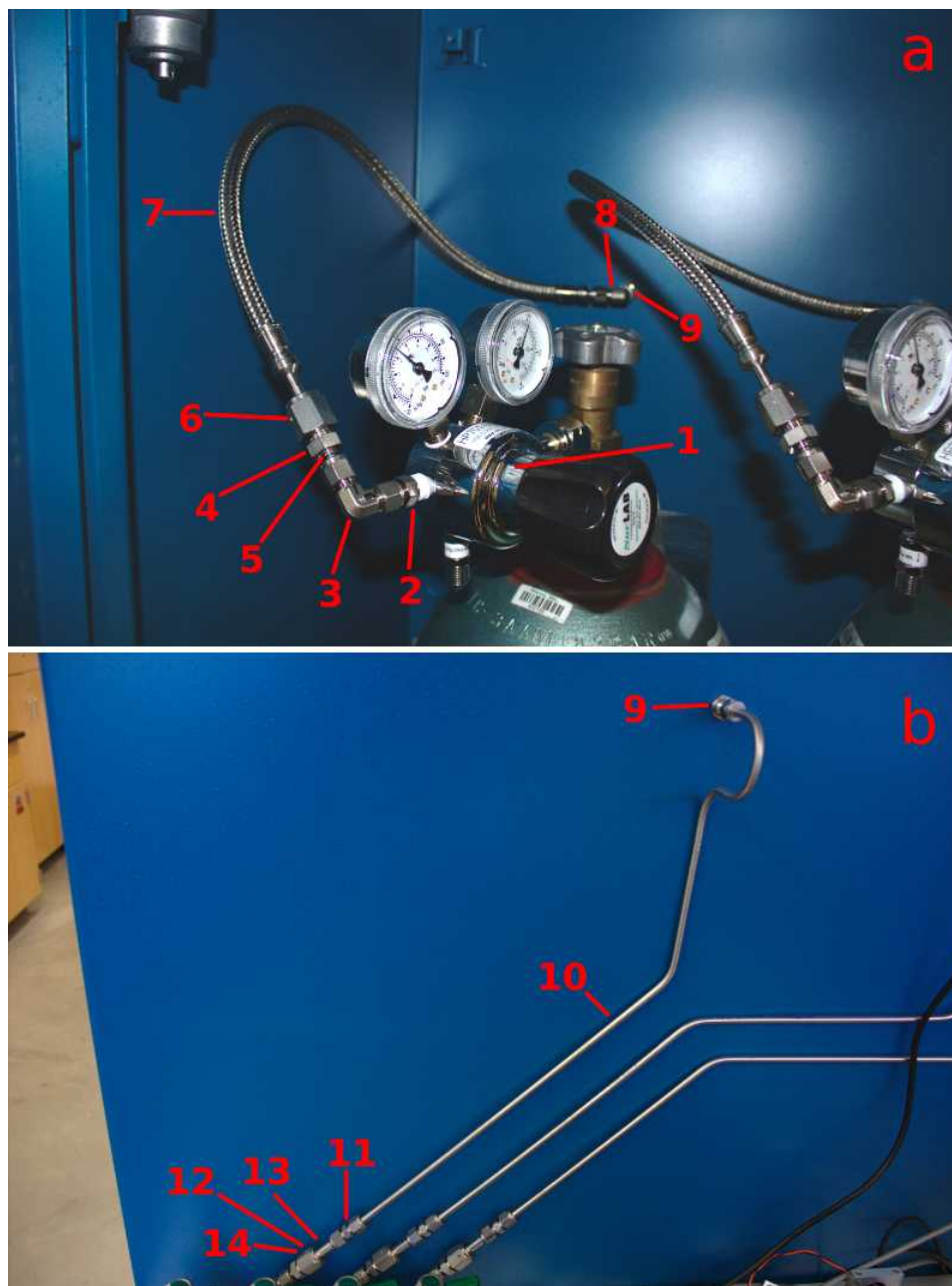


Figure 3.2 Gas delivery line. Views show a) the inside of the gas cabinet and b) on the back side of the gas cabinet.

3.1.2 Gas Filter Lines

Following the gas delivery lines are the gas filter lines (Figure 3.3). Here there are manual diaphragm valves for each gas (part 5), as well as a two-stage filter, 2 micron (part 7) followed by a 3 nm ultra high purity filter. Note: The filters used in our final system, and shown in the image, were phased out of the final design because of their high cost, but they are functionally equivalent to those in the final design.

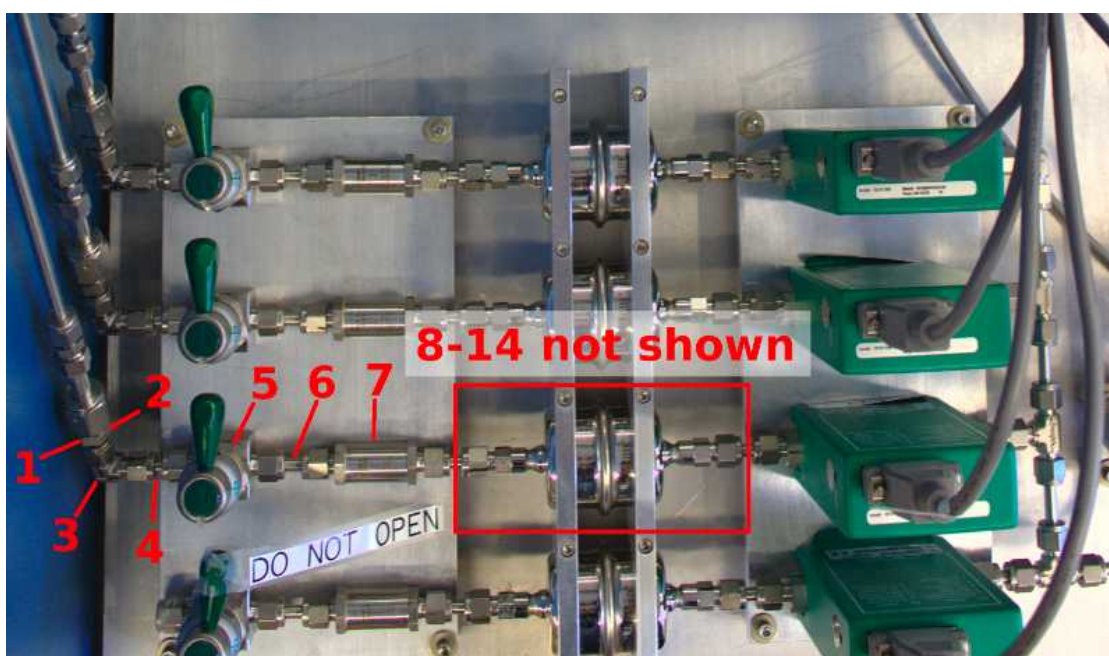


Figure 3.3 Gas filter lines. MFCs are shown at the right.

3.1.3 Mass Flow Controllers

The mass flow controllers (MFCs) chosen were the M100 series from MKS Instruments (Figure 3.3, right side of image). Flow rates were chosen to be 1000 sccm for argon and methane, 500 sccm for hydrogen, and a 20 sccm MFC was additionally installed for future expansion.

3.1.4 Gas Mixing Line

As seen in Figure 3.4, the gases exiting the mass flow controllers are mixed in $\frac{1}{4}$ inch tubing via Swagelok union fittings and hand-cut $\frac{1}{4}$ inch stainless tubing. The mixed gases are then routed through a manual diaphragm valve (part 6) and connect to the intake manifold via a VCR to KF25 adapter. The diaphragm valve is useful for system seal check and leak isolation as it isolates the MFCs and everything upstream from the remainder of the system.

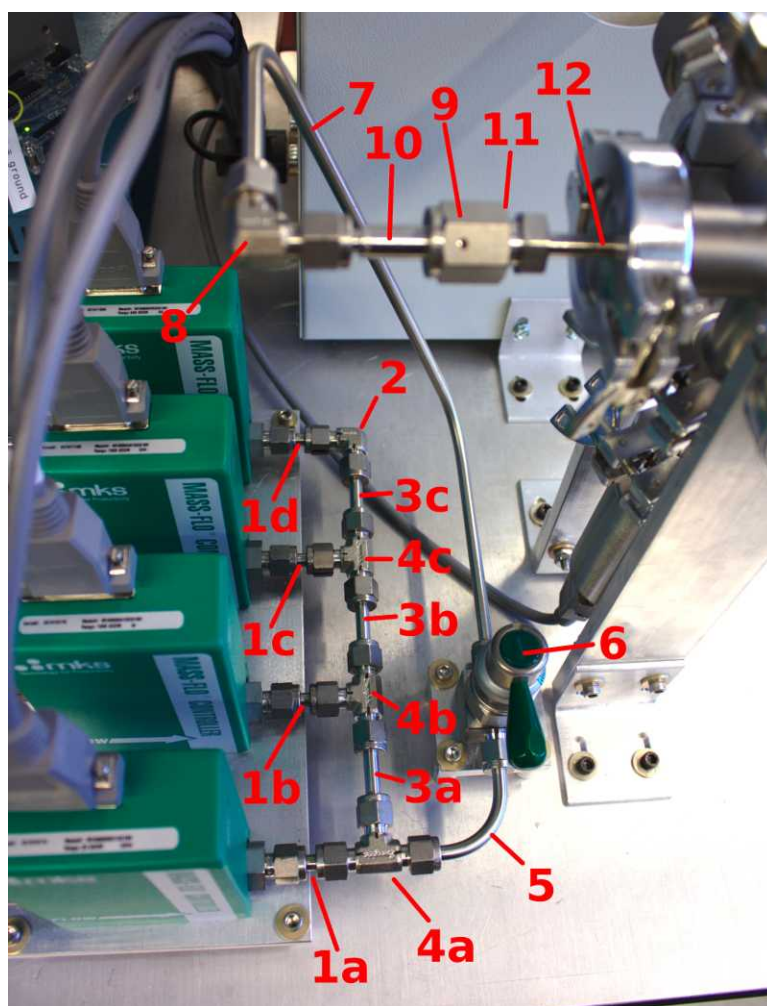


Figure 3.4 Gas mixing line.

3.1.5 Intake Manifold

The intake manifold consists of a KF25 6-way cross (Figure 3.5). One flange is used to deliver the process gases, two flanges (the top and bottom) are used for pressure gauges, one flange connects to the process tube, and two flanges are available for future expansion.

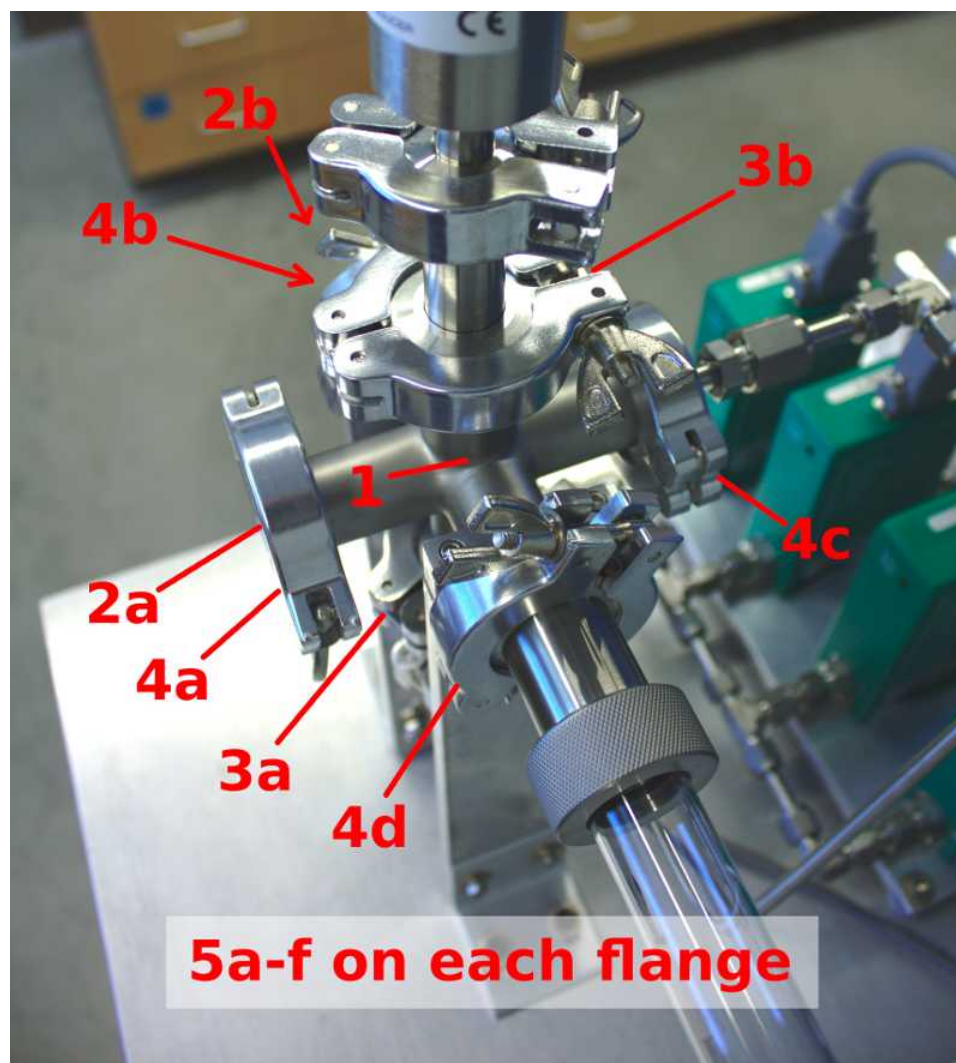


Figure 3.5 Intake manifold.

3.1.6 Pressure Gauges

For low pressure CVD applications, two capacitive manometers were used (Figure 3.6), one with a 1000 Torr full range (part 5) and the other with a 10 Torr full range (part 4). These manometers are connected to the intake manifold via KF17 to KF25 adapters (parts 1a, 1b), and can be moved to other KF25 fittings throughout the system to aid in leak localization.

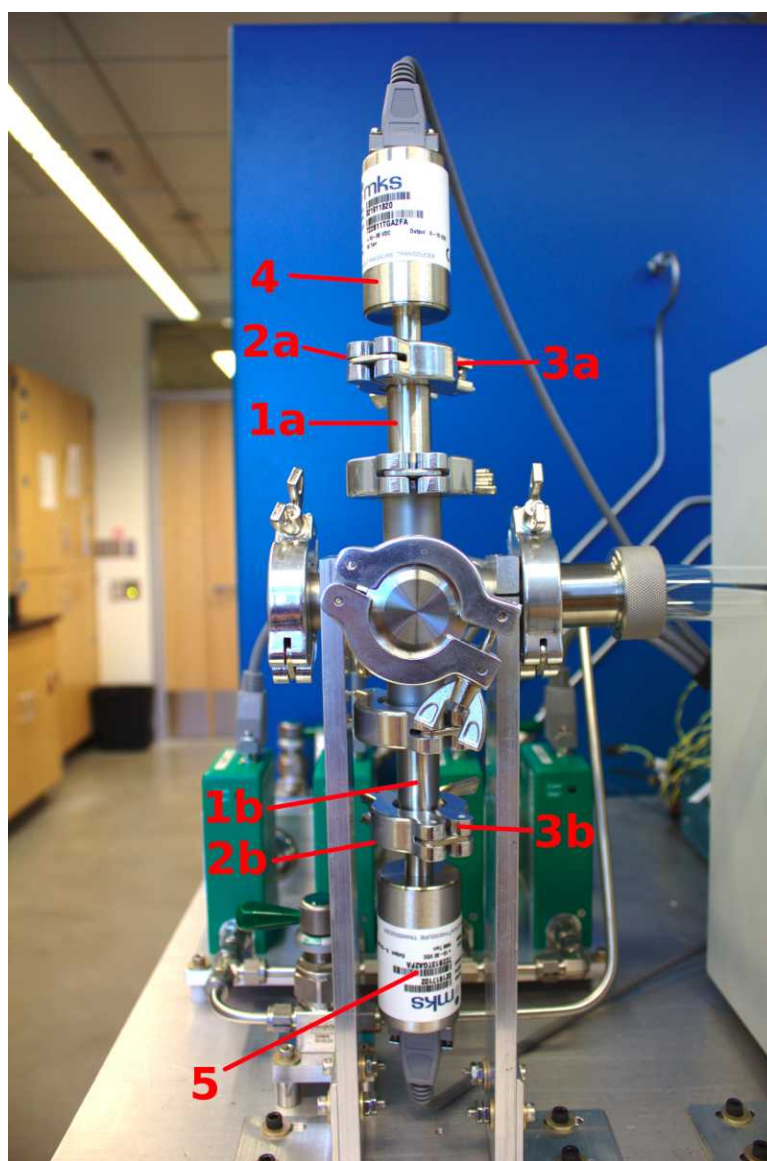


Figure 3.6 Pressure gauges.

3.1.7 Reaction Tube

The reaction tube assembly is shown in Figure 3.7. The reaction tube is a 24-inch long, 1 inch outer diameter sintered quartz tube (part 2) that is coupled to the intake manifold via a KF25 to 1-inch quick disconnect (part 1) and the exhaust manifold via a 1-inch to KF40 quick disconnect. Tubes with fire-polished ends should be used to lower the likelihood of tube breakage during handling.

The tube assembly can be removed via the loosening of the quick disconnects from the tube, then the removal of the KF cast clamps that couple the quick disconnects to the intake and exhaust manifolds. Quick disconnects can then be slid toward the center of the tube and the whole tube assembly can be lifted away from the system.

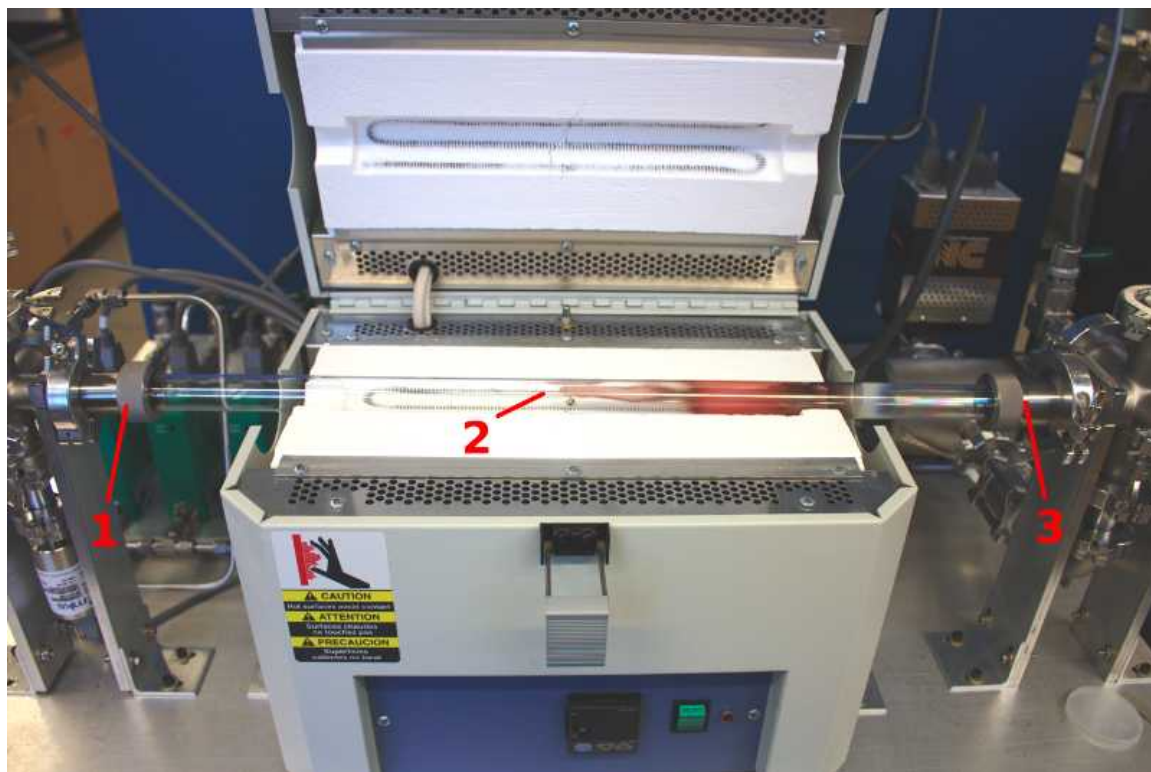


Figure 3.7 Reaction tube assembly. Coloration downstream of the furnace center is mainly due to copper deposition from graphene growths.

3.1.8 Furnace

The furnace is a Lindberg/Blue M Mini-Mite Tube Furnace (Figure 3.8). This furnace accepts a 1 inch outer diameter tube and can operate at temperatures up to 1100°C. Control is possible with the controller seen on the front of the furnace, or via a serial connection. The temperature and setpoint are displayed on the front panel during operation via either method.

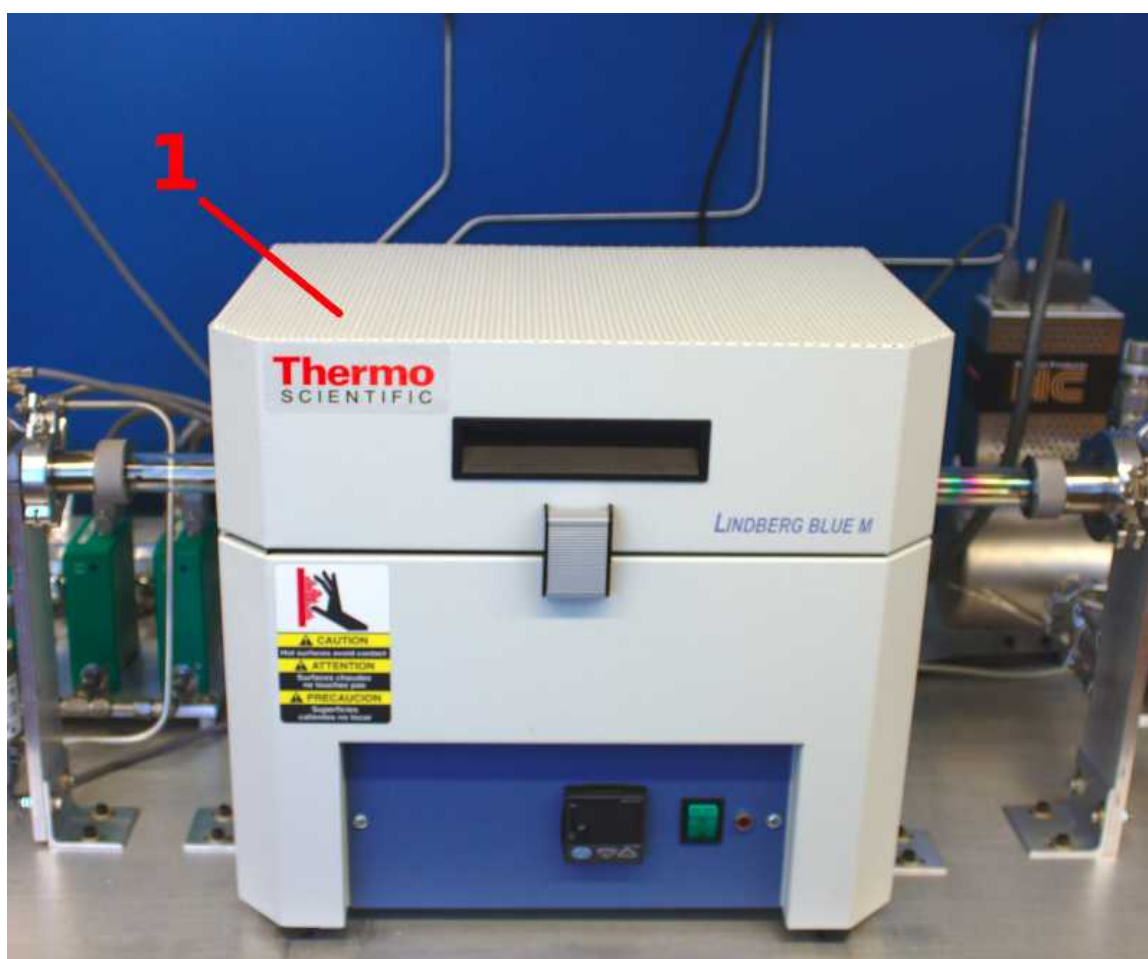


Figure 3.8 Tube furnace.

3.1.9 Exhaust Manifold

The exhaust manifold (Figure 3.9) is based around a KF40 6-way cross (part 1). The flow goes into the exhaust manifold from the reaction tube assembly and out via the exhaust line connected to the bottom flange. The upper flange is used for an overpressure relief line, while the back flange holds a manual venting valve. Two ports are unused and available for future expansion.

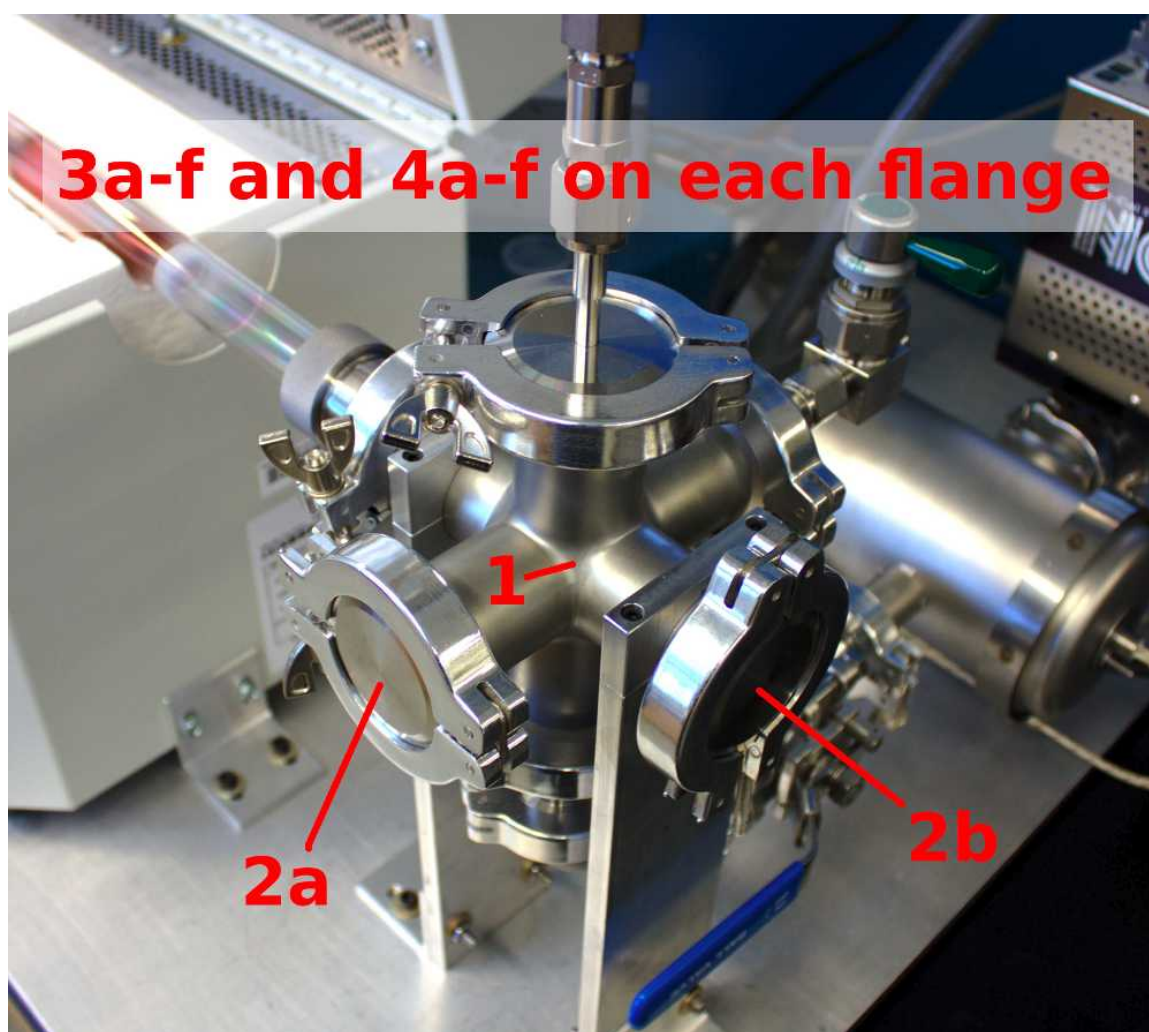


Figure 3.9 Exhaust manifold.

3.1.10 Overpressure Relief

The max system pressure is regulated via an overpressure relief line (Figure 3.10). Part 3 is a poppet check valve with a 1 psi cracking pressure. Part 8 is a ¼ inch hand-bent stainless tube going from the system to the snorkel manifold. This is the main overpressure safety component, limiting the system pressure to below 1 psi above the pressure in the building exhaust line pressure.

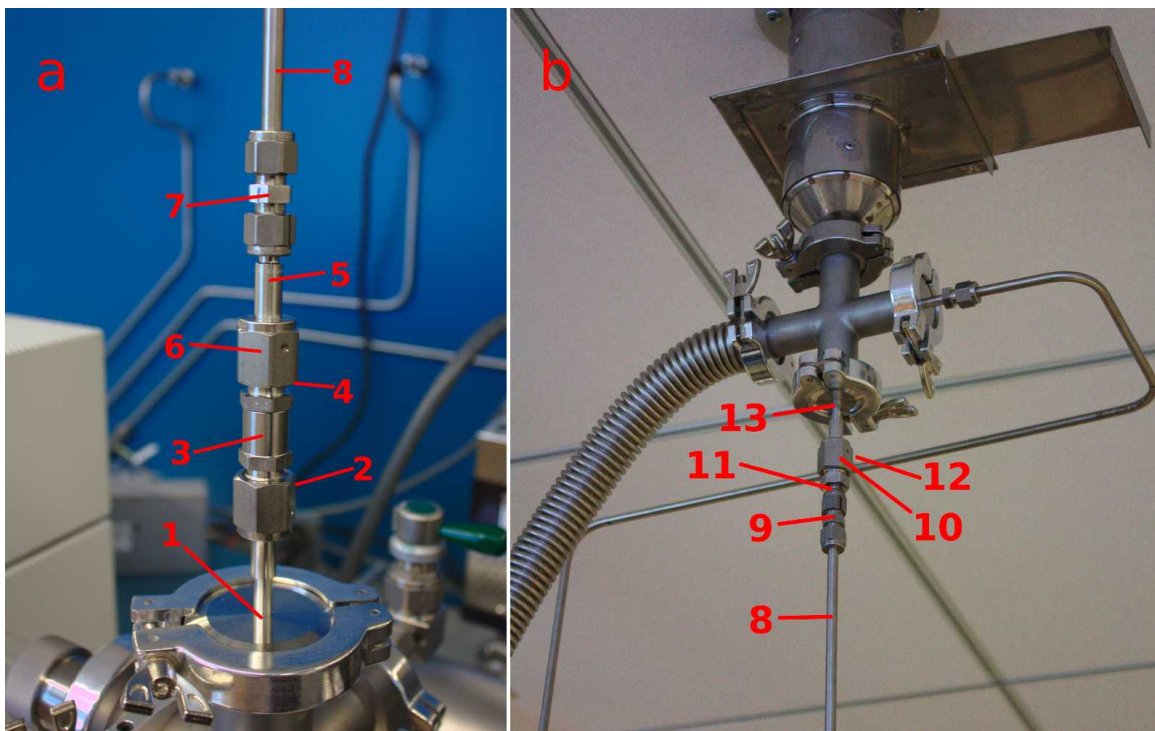


Figure 3.10 Overpressure relief line. a) Connection to top of exhaust manifold. b) Connection to room's exhaust snorkel.

3.1.11 Vent Valve

The vent valve sits on the back side of the exhaust manifold (Figure 3.11). The vent is a manual diaphragm valve (part 3) used to equilibrate the system pressure with the room pressure before breaking the system seal. With normal, automated system use the vent valve will not need to be used as the automated controls automatically repressurize the system to slightly above room pressure after each run.

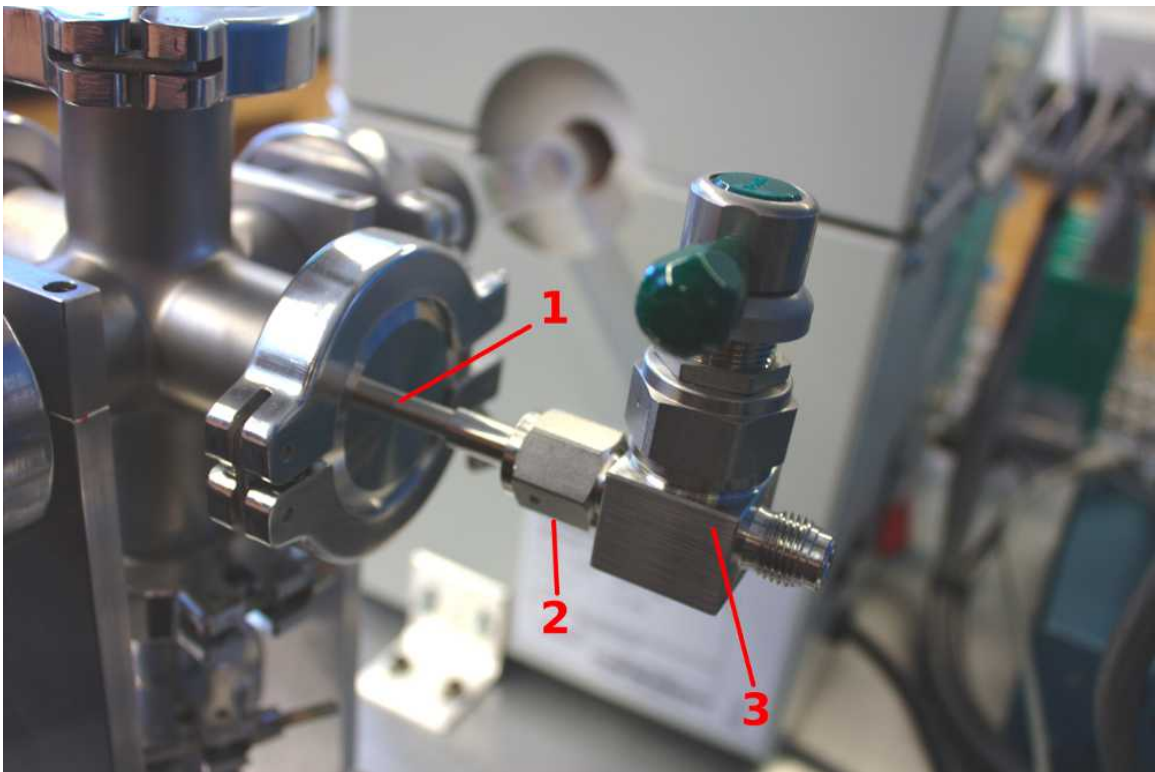


Figure 3.11 Vent valve assembly.

3.1.12 Exhaust Line

Connecting to the bottom flange of the exhaust manifold is the exhaust line (Figure 3.12). The exhaust line contains a ball valve for leak isolation (part 7), a molecular sieve filter (part 10), and a slot for the butterfly valve, which is its own subsystem. The filter can be heated via a standard wall socket to drive out volatiles.

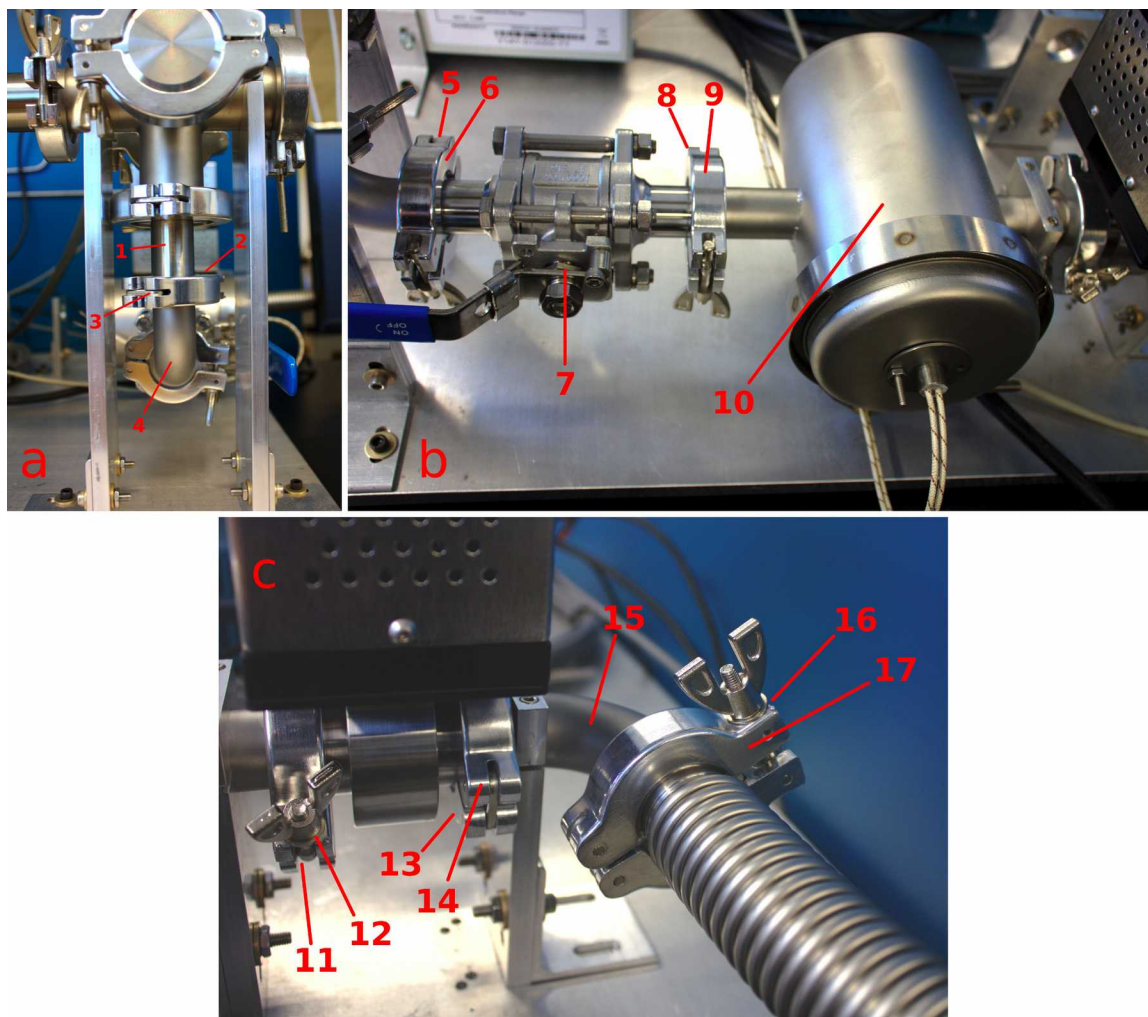


Figure 3.12 Exhaust line. a) shows how the exhaust line is coupled to the exhaust manifold via a KF40 to KF25 adapter (part 1). b) shows the ball valve (part 7) and filter (part 10), while c) shows where the butterfly valve is integrated into the exhaust line.

3.1.13 Butterfly Valve

Contained within the exhaust line is the butterfly valve (Figure 3.13). Both pressure gauge readings feed into the valve's integrated controller and the valve uses the downstream vacuum to match the system pressure to a software-controlled setpoint. The butterfly valve is situated downstream of the filter in order to avoid deposition of effluent on the valve hardware.

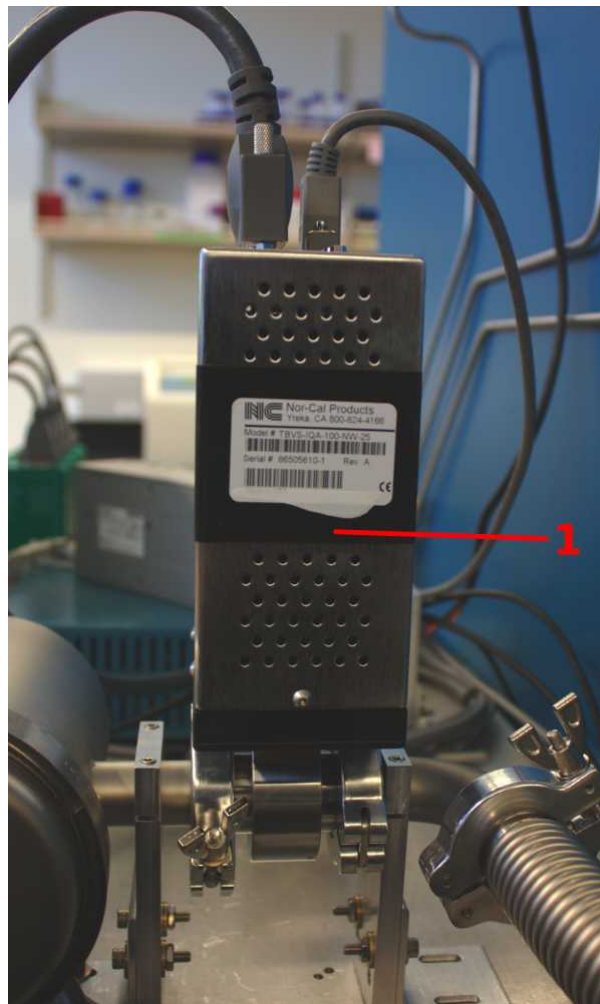


Figure 3.13 Butterfly valve.

3.1.14 Vacuum Pump

The vacuum pump subsystem is shown in Figure 3.14. The system is connected to the vacuum pump (part 4) via KF25 bellows (part 1). The exhaust of the vacuum pump is routed to the snorkel manifold via a second bellows (part 7).

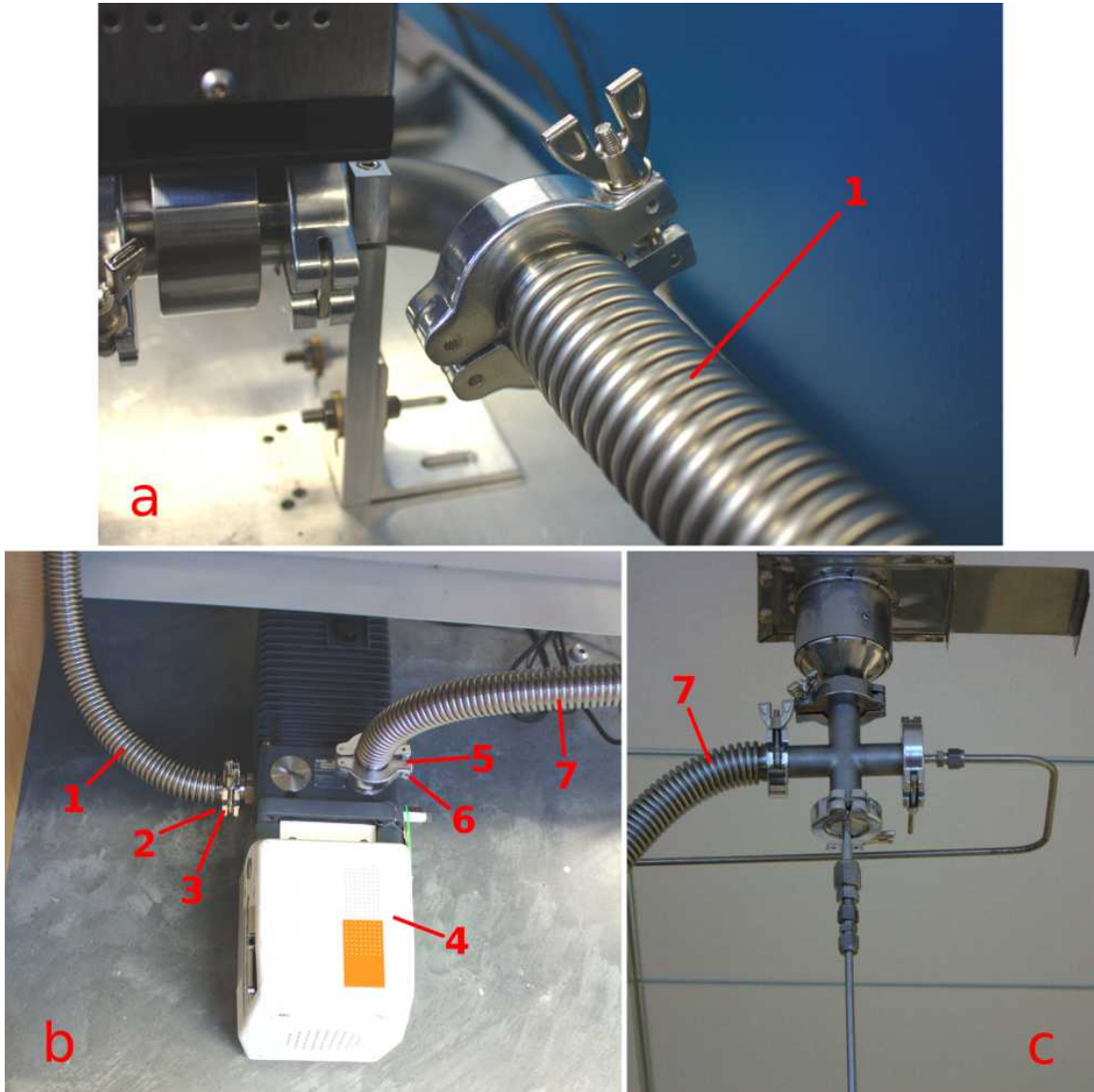


Figure 3.14 Vacuum pump subsystem.

3.1.15 Snorkel Manifold

The snorkel manifold (Figure 3.15) connects to the lab's exhaust port, allowing for the connection of multiple lines to the building's exhaust. In the case of this CVD design, two ports are used, one for the bellows from the exhaust side of the vacuum pump and the other for the overpressure relief valve. The third port is used by another piece of equipment in the lab. A 6-way cross might be considered if additional exhaust ports are needed in a room.

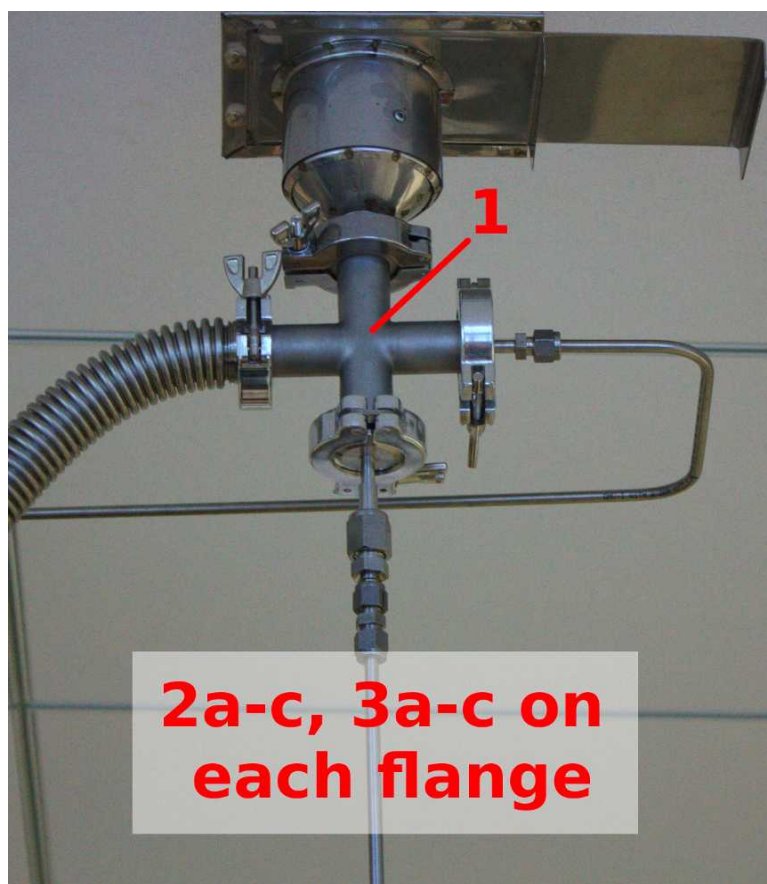


Figure 3.15 Snorkel manifold.

3.1.16 Cables

Active hardware components were chosen with DB-type connectors, so cabling consisted largely of DB cables that had been severed at one end for individual wire access. Figure 3.16 shows cable management and the construction notes have detailed instructions for the fabrication and connections of each cable.

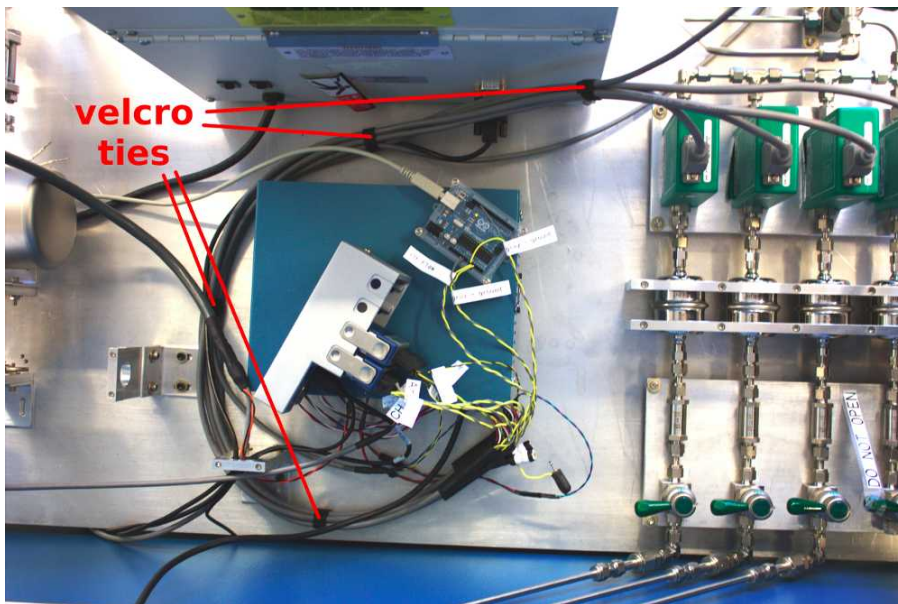


Figure 3.16 System overview showing cable management.

3.1.17 Data Acquisition and Control

While communication with the furnace and butterfly valve was carried out via serial, the MFCs and Baratrons required analog inputs and outputs. These were supplied via a National Instruments CompactDAQ data acquisition system (Figure 3.17, part 1). The final design uses one 16-channel analog input module (part 2) and two 4-channel analog output modules (parts 3a, 3b). The high cost of this system may be reason to explore other options for both data acquisition boards and active hardware (MFCs, Baratrons) for future builds.

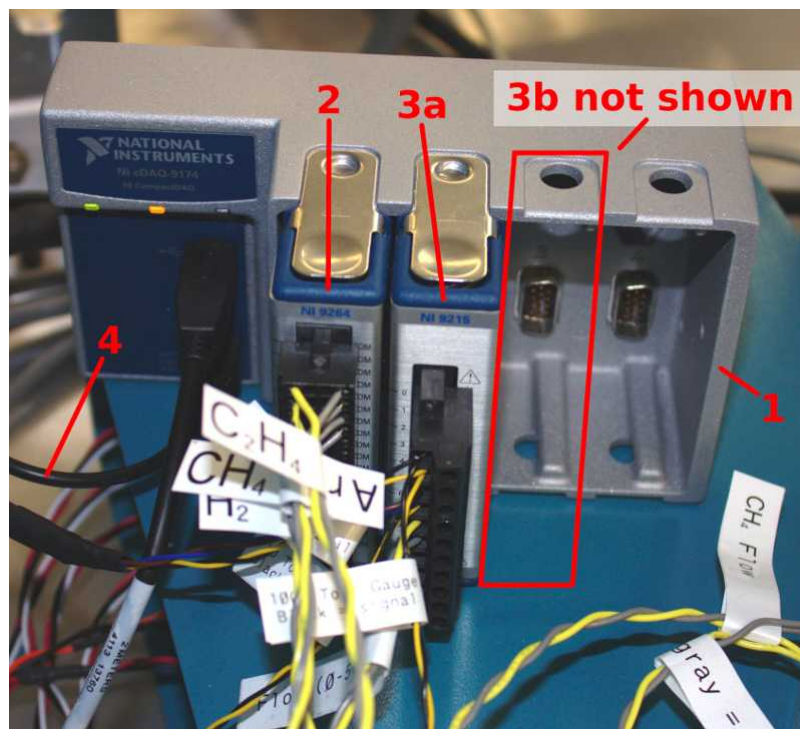


Figure 3.17 National Instruments cDAQ system with 2 modules. Note: An additional analog output module (part 3b) was added to the final design but not to our system.

3.1.18 Base and Supports

The base was fabricated from a ½-inch aluminum plate 30 inches wide by 42 inches long (Figure 3.18, base). The edges and corners of the base were rounded with a file and sandpaper, then 8 rubber feet were distributed across its underside.

Gas filter line, MFC, and gas mixing line hardware was attached to the base via machined aluminum 3/8 inch plates, as seen in Figure 3.18b (part 8). These are held off with spacers (part 2) so that cap screws can secure the parts from the bottom of the support plate. Reference designs of the support plates can be found in the supplementary material.

KF components including the intake manifold, exhaust manifold, and exhaust line were supported via vertically oriented aluminum support structures (Figure 3.18c). The parts are clamped into the support structure via a pair of cap screws (Figure 3.18c, part 9) and the support structure is secured to the base plate via a piece of machined angle aluminum (part 10). Slots in the angle aluminum pieces allow for some play in the height and location of the support piece, while the system configuration can be completely changed via the drilling and tapping of new holes in the base plate.

The furnace was secured to the base plate via a pair of angle aluminum brackets (Figure 3.18d, part 10). This ensures that the furnace will not move during a growth and break the stationary reaction tube contained within it. The furnace's face plate had to be removed before holes were drilled into the furnace body to ensure that no internal components were damaged.

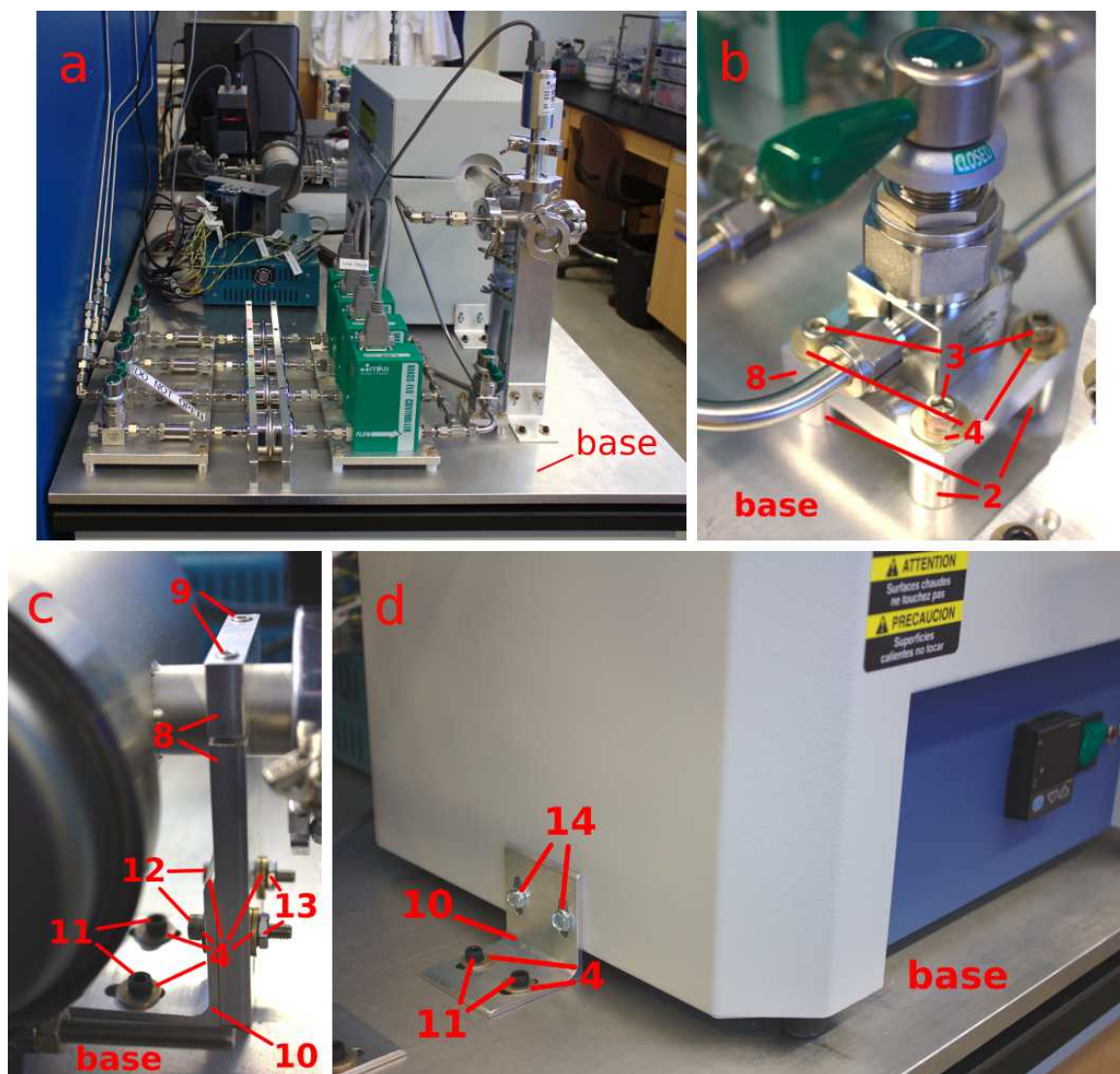


Figure 3.18 Base plate and support structures. a) Base plate in a system side view. b) Details of a manual valve support structure in the gas mixing line. c) Close up of a support for the molecular sieve filter. d) One of two securing brackets for the furnace.

3.2 Driver and Software Design

Once a sample is prepped and placed into the reaction tube, the manual gas line and gas mixing valve are turned on, the furnace is turned on, and the vacuum pump is started, all system control is conducted on a PC running LabView. The main elements of the controls programming are the device drivers, the manual control program, and the automatic control program. Detailed system startup instructions are given in the construction notes in the supplementary material.

3.2.1 Device Drivers

Contained within the 'Programs/sub-VIs' folder of the supplementary materials folder, the device drivers are small LabView programs that operate the system's active hardware (MFCs, pressure gauges, furnace, and butterfly valve). These driver programs can be opened and tested individually in order to test the operation of single active components. Or, in the case that the system design is modified, the drivers for the modified components can be reprogrammed independently, making it simple to modify the system design to fit a lab's individual needs.

3.2.2 Manual Control Program

The manual controls LabView VI, called 'ManualControls.vi' is located in the 'Programs' folder of the supplementary material. A screen capture of the user interface is shown in Figure 3.19. Once the system has been built and the active components tested, the manual controls VI can be used to check system seal and run simple growths. When the manual control program is in use, both setpoints and actual values for the system pressure, furnace temperature, and gas flow rates will be recorded in a dated log file.

Because the active hardware components are controlled via sub-VIs,

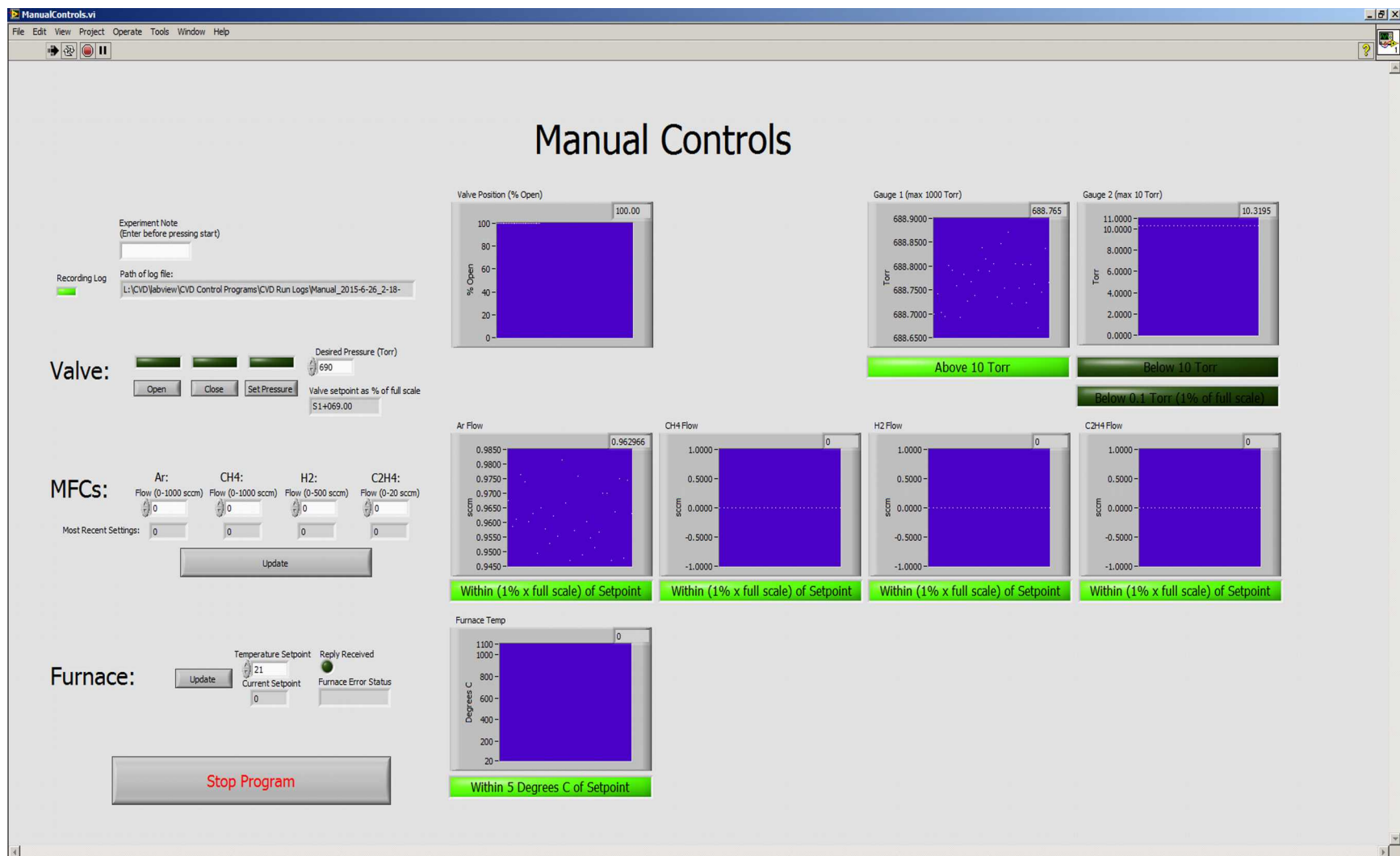


Figure 3.19 Screen capture of the ManualControls.vi control interface. Using this VI the pressure or valve state, gas flow rates, and furnace temperature can all be set and monitored.

modifications to the system design that include different active components than those described in this design should not affect the operation of the manual control program as long as the individual device drivers are updated.

3.2.3 Automatic Control Program

For complex recipes and repeatable growths, the automated control program should be used. Called 'Read&RunRecipe.vi' and contained with the 'Programs' folder of the supplementary materials, the automatic control program operates the CVD according to user-generated recipes. A sample recipe, 'Quick.csv', is included in the 'Programs/Recipes' folder of the supplementary materials. The contents of the comma separated value (csv) file is shown in Figure 3.20. Recipes are organized into stages, and the stages of the sample recipe are as follows: Stage 0 sets the initial setpoints and then immediately ends. Stage 1 ends when the furnace temperature reaches 200°C. In stage 2, the temperature setpoint will ramp from 200°C to 500°C at a rate of 30°C/min and the stage will end once the furnace reaches 500°C. Stage 3 lasts for 10 minutes, and stage 4 ends when the furnace cools to 100°C. After this, the CVD is repressurized with argon and the program stops. The pressure and gas flow rates are set at the beginning of the stage. A line is shown for a fourth gas (C₂H₄) for future system expansion.

Stage	0	1	2	3	4
Pressure Setpoint (Torr)	680	500	300	0	680
Temperature Setpoint (C)	25	200	500	500	25
Temperature Ramp Rate (C/min, 30 C/min max)			30		
Ar Flow (sccm)	0	600	0	0	500
CH ₄ Flow (sccm)	0	0	400	0	0
H ₂ Flow (sccm)	0	0	0	200	0
C ₂ H ₄ Flow (sccm)	0	0	0	0	0
Dwell Time (min)				10	
Stage End Condition	Start	Temp	Ramp	Time	End

Figure 3.20 Contents of the Quick.csv recipe.

Once the recipe is created and saved as a .csv file, the automatic controls program is started and the recipe selected in the file dialog. After the recipe has been selected, the first tab of the controls program will show a simulation of the recipe. The plots generated from this simulation can be seen in Figure 3.21. The top three plots show the projected pressure, temperature, and gas flow rate setpoints vs. stage number, while the bottom three charts show the same values vs. approximate elapsed recipe run time. During the generation of these simulated run graphs, the software also analyzes the recipe to determine if all recipe stages are within the system's allowed setpoints. If the recipe checks out, the square green indicator on the right lights up and the user is able to click the 'Run Recipe' button.

On successful recipe check and clicking of the 'Run Recipe' button, the user can then move on to the next program tab to see the process of the system check. Prior to executing the user's recipe, the automatic control program will conduct a system check to ensure that the furnace and butterfly valve are replying over serial, the gases required for the recipe are available, the system is sealed, and the vacuum pump is operating. In the case that any of these checks fail, the system is repressurized to room pressure with argon and the program is stopped. A screen capture of the controls program after a successful system check is shown in Figure 3.22.

If the system check is successful, the program will begin to run the recipe and the user can continue to the next program tab to monitor the recipe's progress. A screen shot of the third tab is shown in Figure 3.23. Here the user can see the setpoints and end condition for the current stage, as well as the current pressure, temperature, and gas flow rates. When the recipe reaches the 'End' stage, it will cool until it reaches 100° C and then

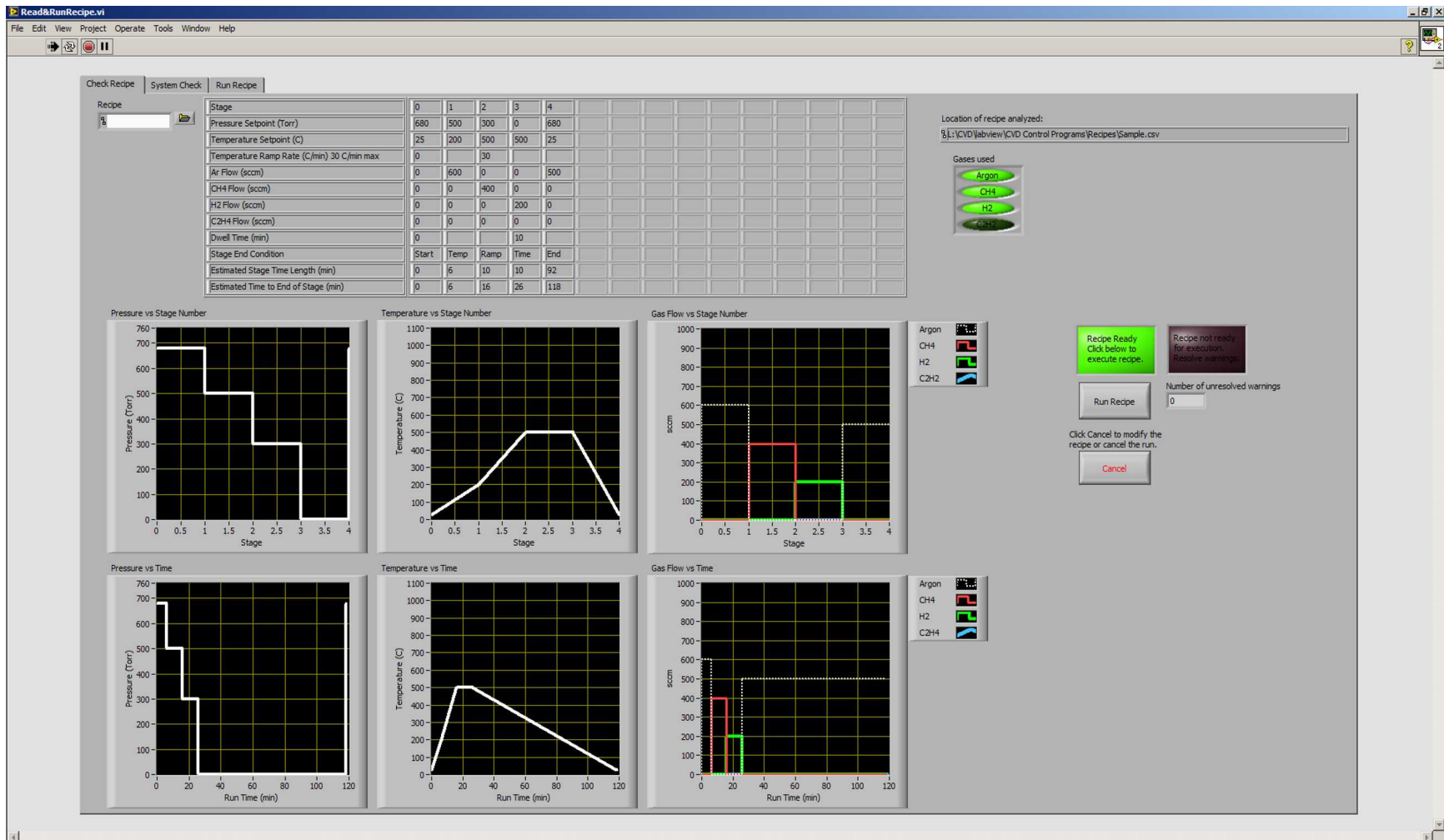


Figure 3.21 Screen capture of the 'Check Recipe' tab of Read&RunRecipe.vi. When the VI is run and a recipe selected, the recipe will be checked and simulated, with the simulated growth profiles appearing in the graphs, plotted by both stage number and estimated growth time. If the growth profiles are acceptable as shown, the user can click 'Run Recipe' to begin the CVD system check.

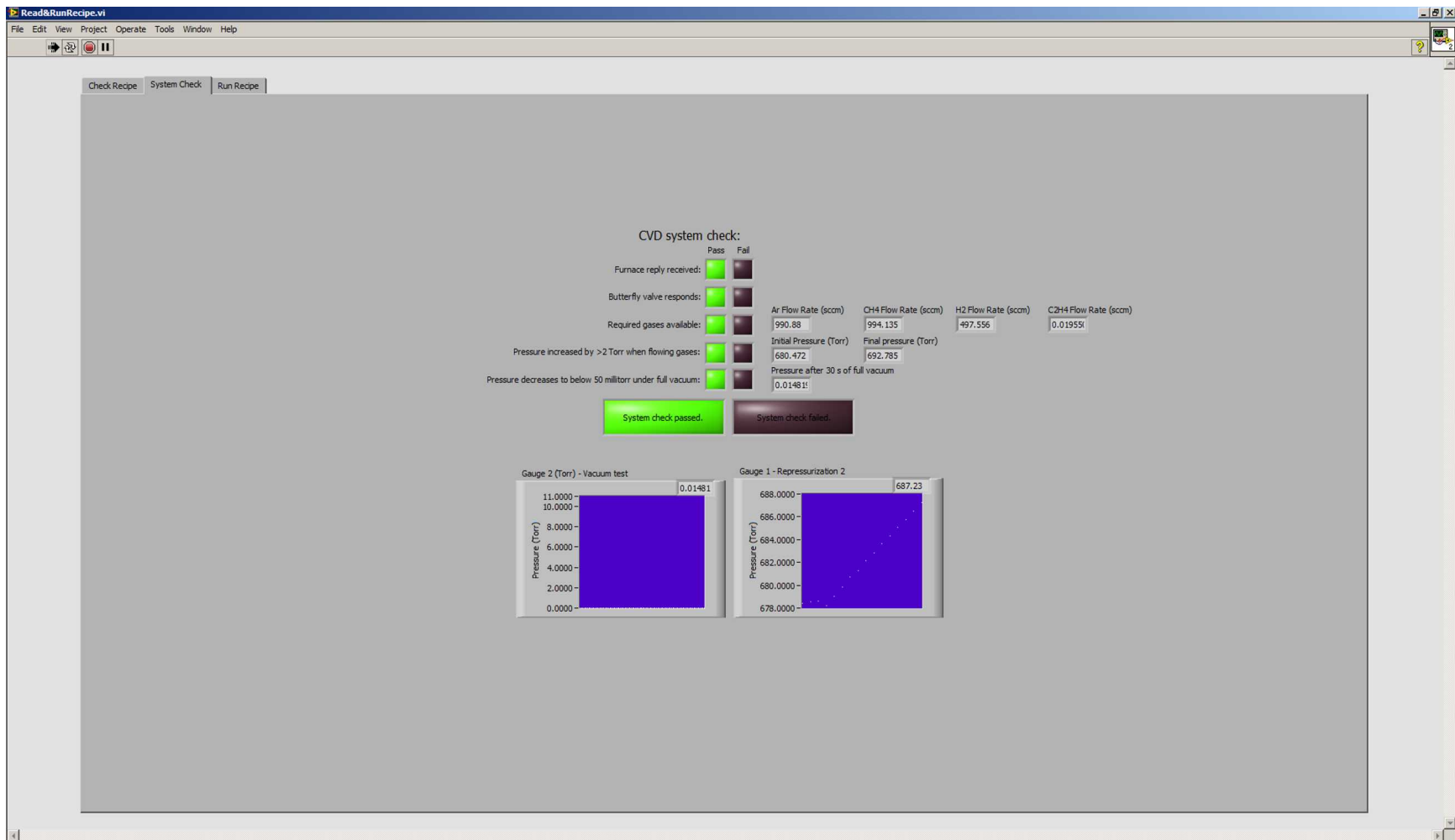


Figure 3.22 The 'System Check' tab of Read&RunRecipe.vi. When a CVD run has been started, the program will first conduct a system check to ensure that the furnace and butterfly valve are responding, the gases required for the recipe are available, the vacuum pump is on, and the CVD is sealed. If the system check succeeds, the user will be prompted for an experiment note then the recipe will start. If the system check fails, the CVD will be refilled with argon to room pressure and the program will end.

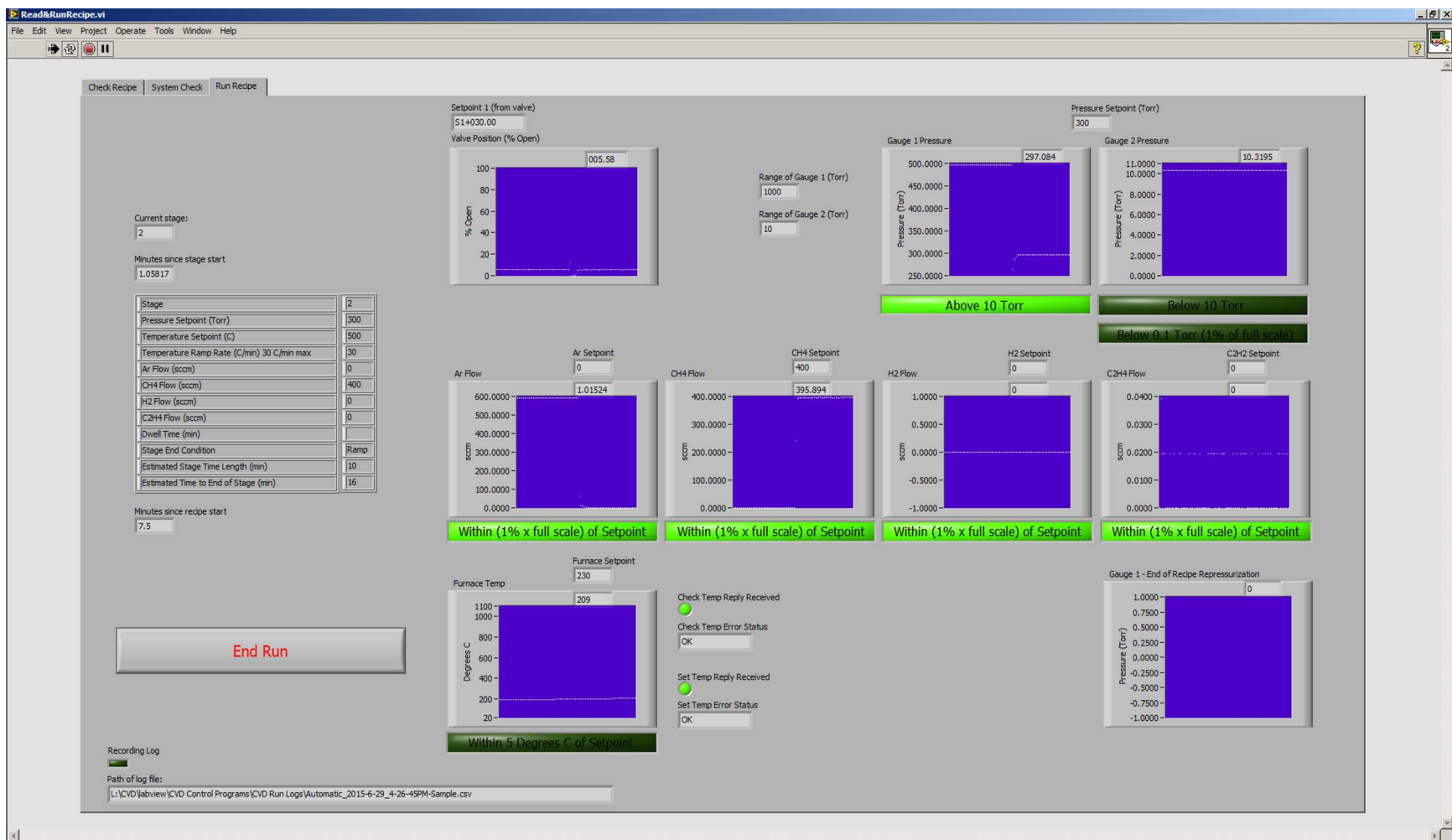


Figure 3.23 The 'Run Recipe' tab of Read&RunRecipe.vi. After the system check has been passed and an experiment note entered, the state of the run can be monitored on this tab. The system state shown is 1 minute after the recipe switched from stage 1 to stage 2. The pressure dropped from ~500 Torr to ~300 Torr, the argon flow rate dropped from ~600 sccm to 0 sccm, the methane flow rate increased from 0 to ~400 sccm, and the furnace temperature setpoint is ramping to 500°C at 30°C/min.

the system will repressurize with argon and stop, leaving the butterfly valve set to a pressure slightly above room pressure to provide a safety against overpressure yet to allow the system to be opened even if the vacuum pump is kept on.

3.2.4 Auditability

Similarly to the manual controls program, the automatic controls program logs both setpoints and actual values for pressure, temperature, and gas flow rates. Additionally, the automated control program saves a copy of the recipe to the 'Programs/CVD Run Logs' folder with the same name as the normal log file but with a '-recipe' suffix. Together, the run logs and the saved recipes allow a researcher to quickly evaluate past growths and provide an audit trail for recipe changes through different growth trials.

In the construction notes, there is additionally an Excel macro that allows one to quickly plot the setpoints and run values of a log file by opening Excel and then using a keyboard shortcut ('Ctrl+g' in this case). The resulting plots for the log file resulting from running the 'Sample.csv' recipe are shown in Figure 3.24. Comparing them to the plots of the predicted run from Figure 3.21, we see that the logged system values matched the predicted recipe profile well, including the temperature ramp as seen on the left side of the temperature plot (Figure 3.24a).

There is noticeable lag in the pressure after sharp increases in the pressure setpoint (Figure 3.24b). This is a result of the limited volume of gas entering the system limiting the rate of pressure increase. Also, the shoulder on the right side of the temperature plot (Figure 3.24a) is a result of the furnace lid being manually opened to increase the cooling rate.

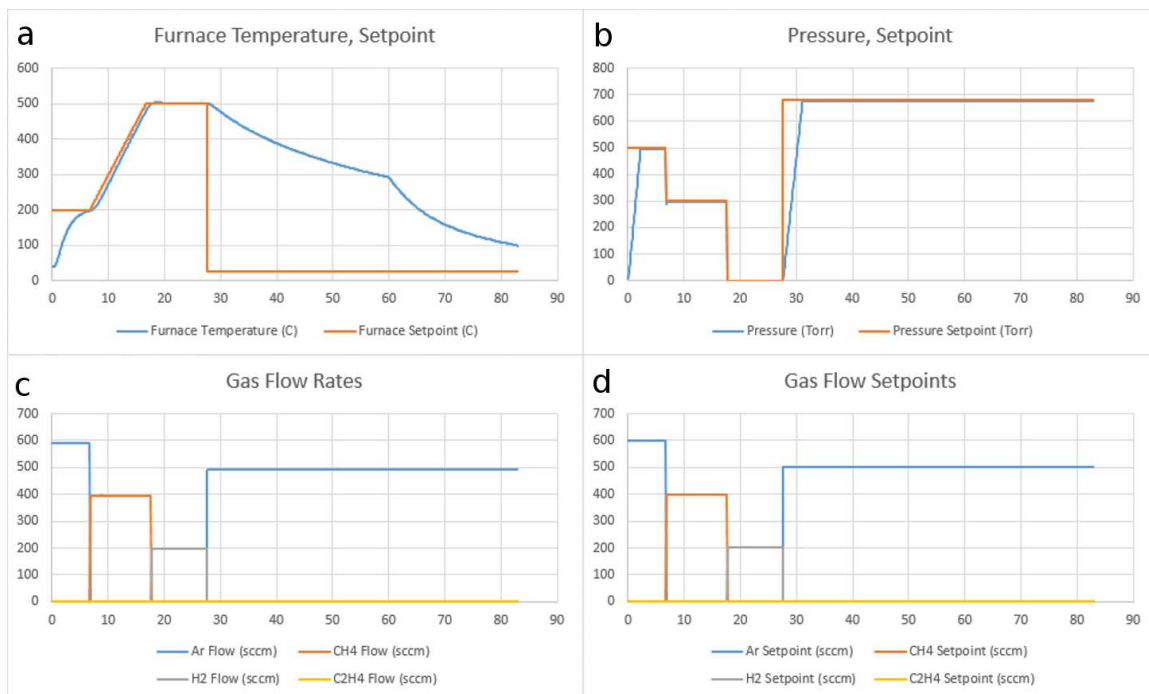


Figure 3.24 Plots resulting from running the Excel macro on the log file resulting from running the 'Quick.csv' recipe. Shown are a) the furnace temperature and setpoint, b) the pressure and setpoint, c) the gas flow rates, and d) the gas flow setpoints.

To test the auditability of the system, the Quick.csv recipe was ran a second time, this time with a user error and a simulation of a gas canister running out. The graphs resulting from running the Excel macro in the run log can be seen in Figure 3.25. At around 9 minutes into the run, the methane valve was closed, and the flow rate can be seen to drop in Figure 3.25c, while the setpoint remains constant in 3.25d. Further, just after the 20 minute mark, we can see in Figure 3.25a that the furnace temperature drops rapidly away from the setpoint, a result of the furnace lid being opened and the heating elements being disabled by the furnace. Finally, as compared to the run logged in Figure 3.24, this run was much shorter, a result of the furnace cooling to the 100°C program shutoff temperature much faster with the furnace open.

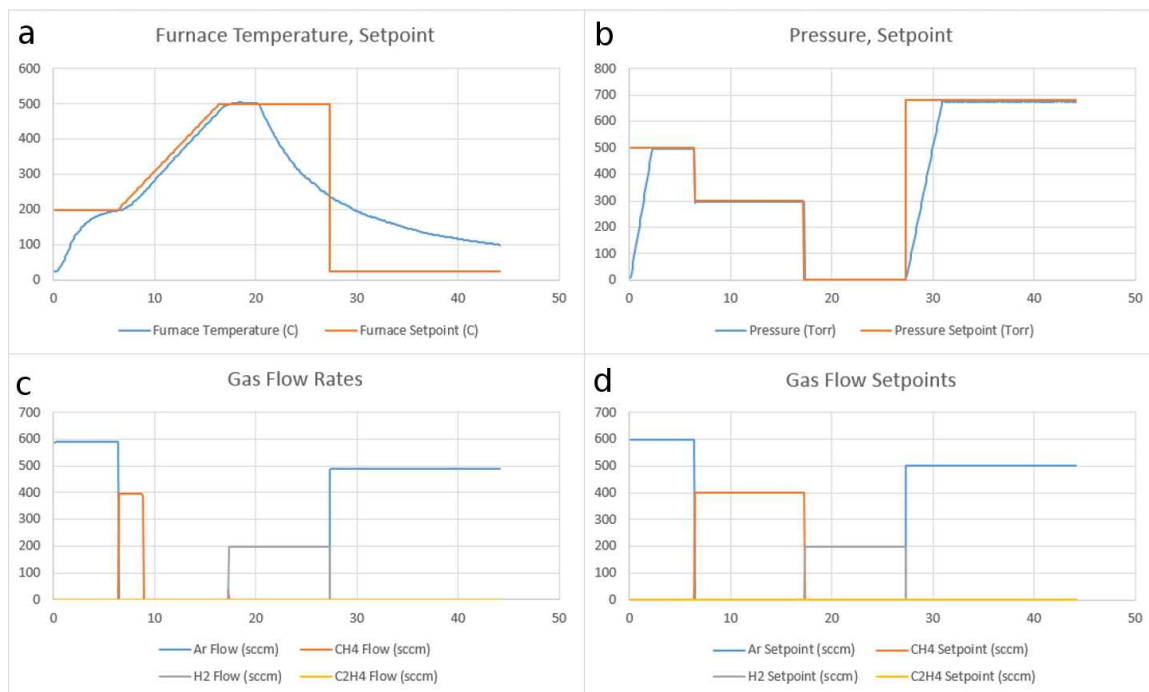


Figure 3.25 CVD run logs for a Quick.csv recipe run during which the furnace was prematurely opened and the methane valve was turned off during the run.

The ability for a user to visually inspect run logs allows for rapid auditing of past runs, giving them the ability to demonstrate consistency and increasing the repeatability of their growths.

CHAPTER FOUR: RESULTS AND DISCUSSION

The CVD system built during this project has become a workhorse for the growth of graphene and graphene foam. This chapter details some example growths and characterization of the resulting materials.

4.1 Graphene

4.1.1 Graphene Growth

The planar graphene was grown by chemical vapor deposition (CVD) method on copper foil via a method adapted from a previously published protocol [1]. The copper foil (99.8%, Alfa Aesar 0.001 inch) was placed into the center of the reaction tube and the recipe shown in Figure 4.1 was executed via the automatic control program.

Stage	0	1	2	3	4	5
Pressure Setpoint (Torr)	1	1	1	1	1	690
Temperature Setpoint (C)	25	1000	1000	1000	400	25
Temperature Ramp Rate (C/min) 30 C/min max increase	0					
Ar Flow (sccm)	0	100	100	100	100	500
CH4 Flow (sccm)	0	0	0	850	850	0
H2 Flow (sccm)	0	0	100	50	50	0
C2H4 Flow (sccm)	0	0	0	0	0	0
Dwell Time (min)	0		90	30		
Stage End Condition	Start	Temp	Time	Time	Temp	End

Figure 4.1 Recipe used for the growth of graphene on copper foil.

On conclusion of the growth, the graphene was coated with a bilayer of PMMA (495 K A2 and 950 K A4). The layers were each coated at 3000 rpm with a 2 minute bake at 200° C. The uncoated side of the copper foil was exposed to an oxygen plasma to remove the graphene on that side and then the copper foil was etched overnight in

Transcene CE-100. The resultant PMMA/graphene film was then transferred to a silicon wafer and given a DI rinse and acetone bath to remove the PMMA.

4.1.2 Graphene Characterization

The resulting graphene on silicon was analyzed with Raman (Horiba Instruments, Edison, NJ) using a 532 nm excitation laser. The resulting spectra minus the bare silicon background for four different locations on the sample are shown in Figure 4.2. The D band at $\sim 1350\text{ cm}^{-1}$ is noticeably small across all readings, suggesting the graphene has a low defect density. Also, the high intensity of the G peak ($\sim 1585\text{ cm}^{-1}$) relative to the 2D peak ($\sim 2685\text{ cm}^{-1}$) indicates that the sample is likely multi-layer as the G peak is much smaller than the 2D peak in Raman spectra of monolayer graphene [2,3]. The peak at $\sim 2440\text{ cm}^{-1}$ appeared with an inconsistent intensity on the bare silicon wafer substrate and

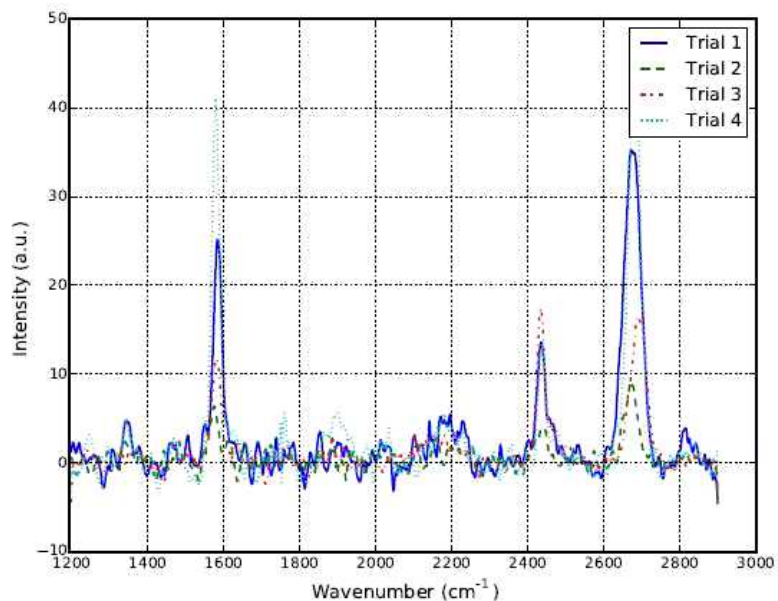


Figure 4.2 Raman of graphene grown in the CVD system described. Trials were taken at 4 different places on the sample. Characteristic peaks at $\sim 1350\text{ cm}^{-1}$, $\sim 1585\text{ cm}^{-1}$, and $\sim 2685\text{ cm}^{-1}$ correspond to the D band, G band, and 2D band, respectively.

is not thought to be a signal from the graphene.

Raman maps were additionally taken of four graphene samples grown using the recipe in Figure 4.1. The ratio of the 2D peak to the G peak heights was mapped, as shown in Figure 4.3. These ratios indicate all four samples consist mostly of mono-layer ($I_{2D}/I_G > 2$) or bi-layer ($I_{2D}/I_G \approx 1.2$) graphene [4]. The laser used for the map had a wavelength of 633 nm with a spot size of $\sim 1 \mu\text{m}$.

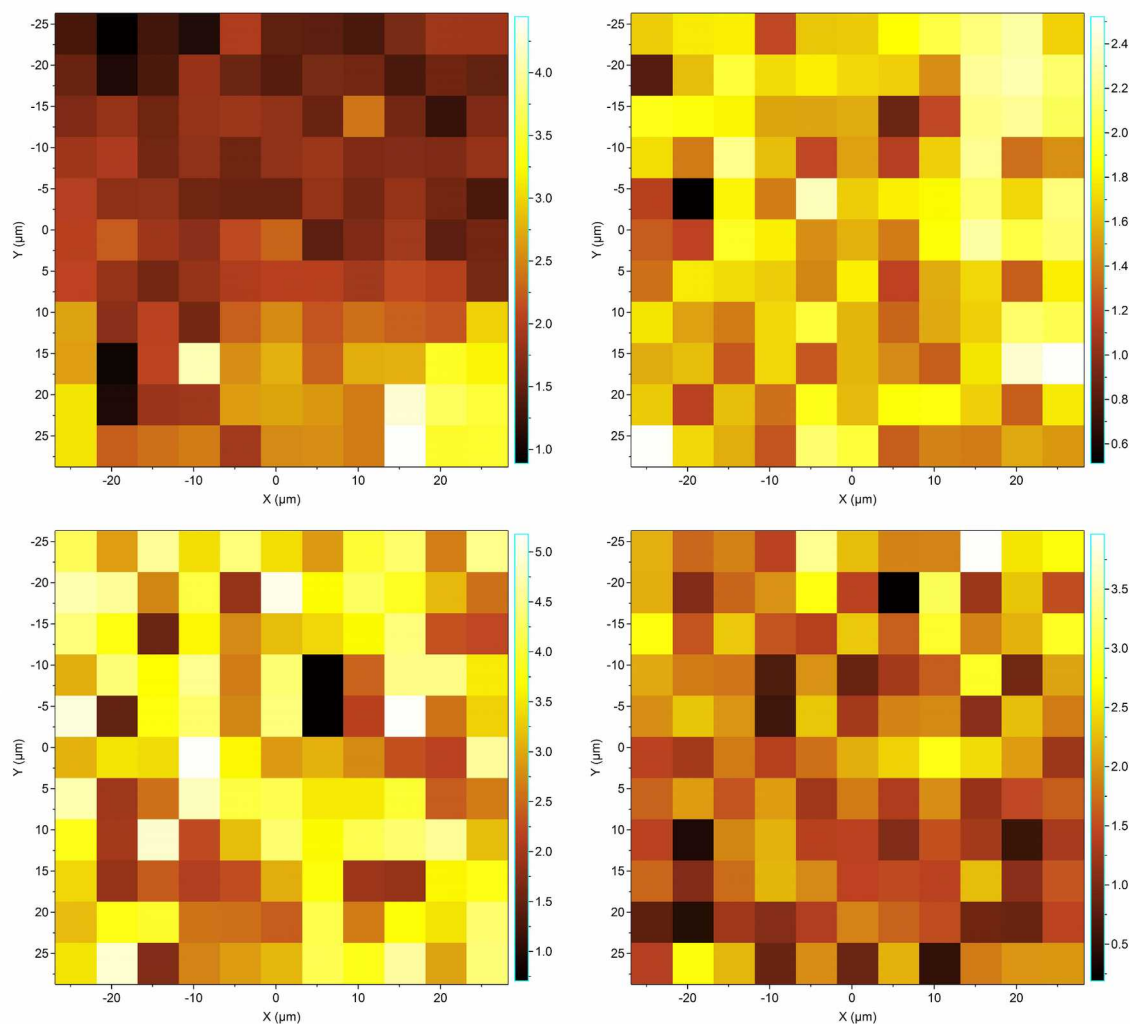


Figure 4.3 Raman maps of four samples grown using identical recipes. Intensity shown is the ratio of the 2D peak height to the G peak height.

The ratio of the area of the G peak to the defect-related D peak was also mapped for the same four areas of the samples, as shown in Figure 4.4. Using this ratio, we can estimate the grain size of the graphene samples using $L_{\alpha} \text{ (nm)} = 2.4 \times 10^{-10} \lambda^4 (I_G/I_D)$, where λ is the excitation wavelength in nanometers [5,6]. Clockwise from the top left, the areas analyzed have average graphene grain sizes of: $L_{\alpha} = 150 \text{ nm}$, $L_{\alpha} = 87 \text{ nm}$, $L_{\alpha} = 77 \text{ nm}$, and $L_{\alpha} = 204 \text{ nm}$. This, along with the result above, indicate that the CVD can produce high quality mono- and few-layer graphene.

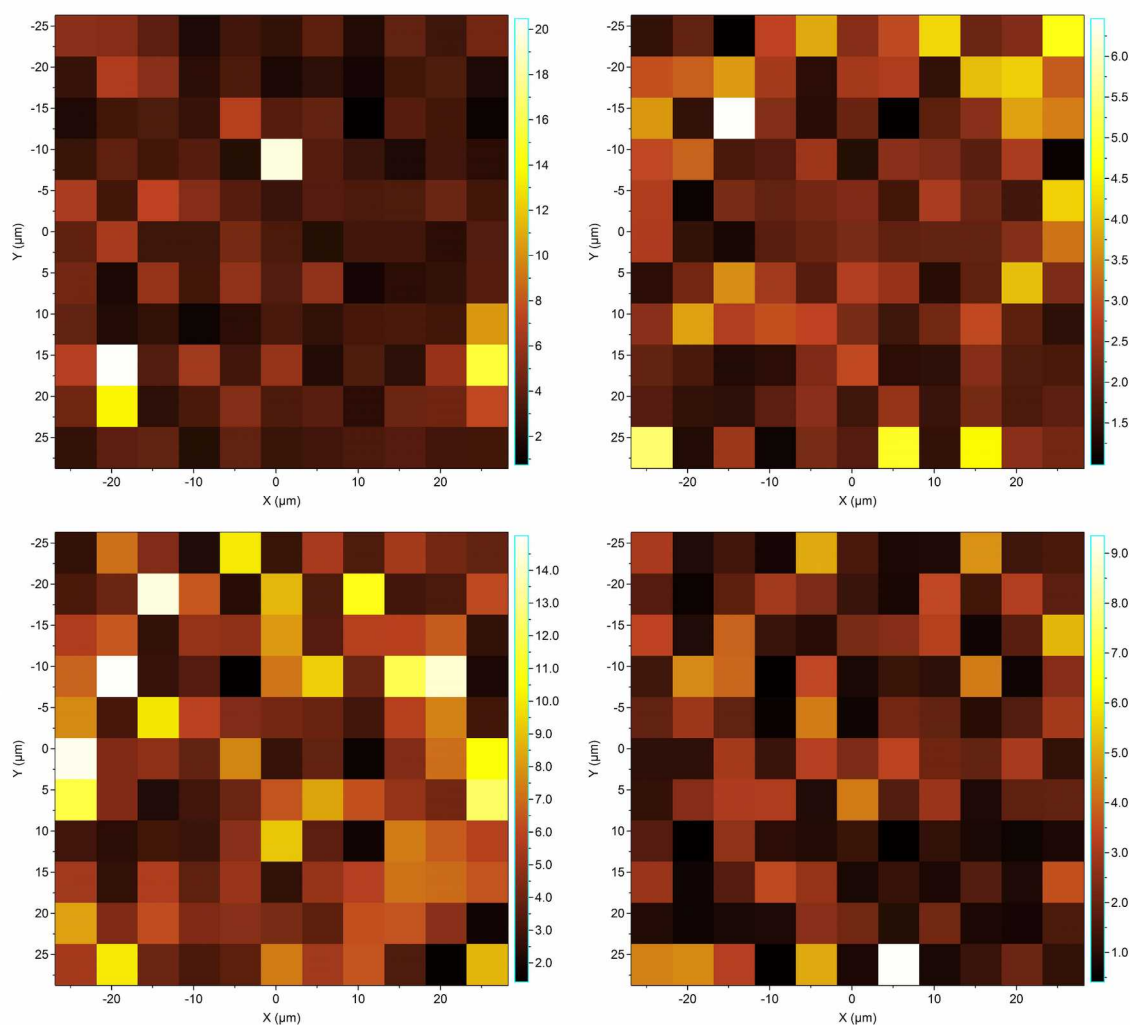


Figure 4.4 Map of the integrated intensity of the G peak to that of the D peak for the four graphene samples.

4.2 Graphene Foam

4.1.2 Graphene Foam Growth

According to a procedure adapted from [7–9], graphene was grown on a nickel foam catalyst (MTI Corporation Porosity $\geq 95\%$, 80-110 PPI, 1.2 mm thick) using the recipe shown in Figure 4.5.

Stage	0	1	2	3	4	5
Pressure Setpoint (Torr)	2	2	2	2	2	690
Temperature Setpoint (C)	25	1000	1000	1000	300	25
Temperature Ramp Rate (C/min) 30 C/min max increase	0					
Ar Flow (sccm)	0	100	100	100	250	250
CH4 Flow (sccm)	0	0	0	50	0	0
H2 Flow (sccm)	0	100	100	100	0	0
C2H4 Flow (sccm)	0	0	0	0	0	0
Dwell Time (min)	0		30	5		
Stage End Condition	Start	Temp	Time	Time	Temp	End

Figure 4.5 Recipe used for the growth of graphene foam onto nickel foam substrate.

The graphene/nickel foam that resulted was coated with PMMA (950A4) and the nickel catalyst was then removed by a 24-hour etch in 1 M FeCl₃/1 M HCl. After transfer to the desired substrate, the PMMA layer was removed in an acetone vapor bath for 20 minutes.

4.2.2 Graphene Foam Characterization

A graphene foam resulting from the described growth with the nickel substrate still present was placed onto a silicon substrate and analyzed via Raman using the same laser line and intensity as was used for the graphene. The resulting spectra from four sites on the sample tested are shown in Figure 4.6. In these spectra, the defect-related D band at $\sim 1350\text{ cm}^{-1}$ is noticeably absent, suggesting high quality graphene with a low concentration of defects. Also, the G band signals at $\sim 1585\text{ cm}^{-1}$ are about the same size

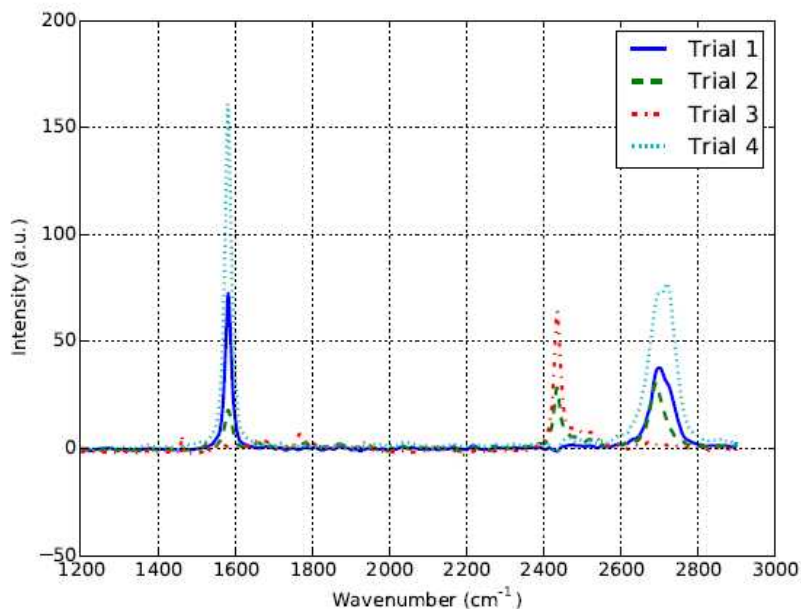


Figure 4.6 Raman of graphene foam on nickel with the background signal subtracted. The defect-related graphene D peak at $\sim 1350 \text{ cm}^{-1}$ is absent in these spectra.

or larger than 2D band at $\sim 2685 \text{ cm}^{-1}$, suggesting these areas were multi-layer. Trial 3 looks to have had a silicon signal that washed out the graphene signal.

The graphene foam was additionally imaged using a scanning electron microscope (SEM) operating at 20 keV (Hitachi S-3400N-II). The resulting images are shown in Figure 4.7. While there was some collapse of the foam structure after etching, as can be seen by comparing Figures 4.7a and 4.7c, the graphene kept much of the structure when the nickel foam was removed. This is consistent with the conclusion reached from Raman analysis that the graphene foam samples consist of multi-layer graphene. Also of note, Figure 4.7b shows apparent wrinkles on the surface of the nickel foam, likely wrinkles in the graphene layers. This wrinkling is consistent with the small thermal expansion coefficient of graphene relative to metals – as the metal foam cools

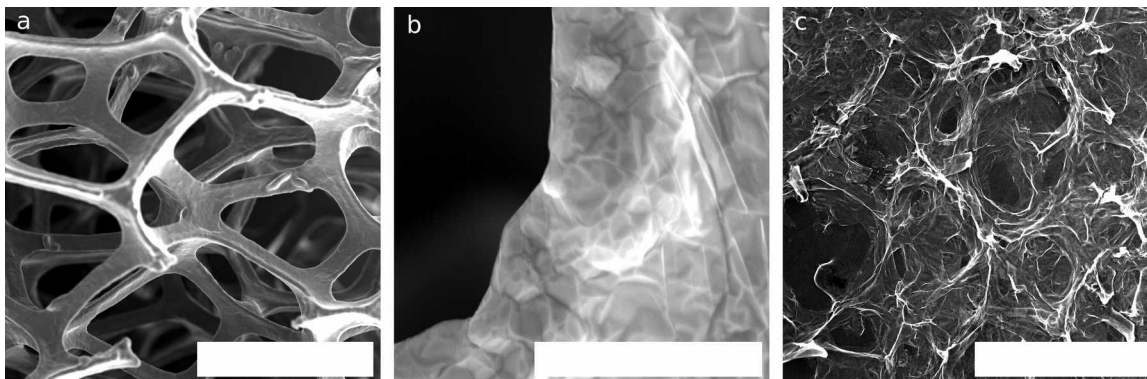


Figure 4.7 a) SEM images of graphene grown on a metal foam. b) Closeup of graphene grown on nickel foam. The apparent wrinkles on the right side of the image are thought to be a result of the metal having a larger coefficient of thermal expansion than graphene. c) Graphene foam after the nickel foam substrate has been etched. Scale bars are 500 μm , 20 μm , and 500 μm , respectively.

after CVD growth of the graphene, it will shrink while the graphene layers coating it will shrink much less.

4.4 References

1. Banerjee S, Shim J, Rivera J, Jin X, Estrada D, Solovyeva V, et al. Electrochemistry at the edge of a single graphene layer in a nanopore. *ACS Nano*. 2013;7: 834–843. doi:10.1021/nn305400n
2. Chen Z, Ren W, Gao L, Liu B, Pei S, Cheng H-M. Three-dimensional flexible and conductive interconnected graphene networks grown by chemical vapour deposition - supplementary information. *Nat Mater*. 2011;10: 424–8. doi:10.1038/nmat3001
3. Bhaviripudi S, Jia X, Dresselhaus MS, Kong J. Role of kinetic factors in chemical vapor deposition synthesis of uniform large area graphene using copper catalyst. *Nano Lett*. 2010;10: 4128–33. doi:10.1021/nl102355e
4. Mohsin A. Graphene synthesis and characterization on copper [Internet]. 2012. Available: <http://ir.uiowa.edu/etd/3354/>
5. Childres I, Jauregui L, Park W, Cao H, Chen Y. Raman Spectroscopy of Graphene and Related Materials. *New Dev Phot Mater Res*. 2013; 1–20. doi:10.1016/B978-0-444-53175-9.00016-7

6. Salehi-Khojin A, Estrada D, Lin KY, Bae MH, Xiong F, Pop E, et al. Polycrystalline graphene ribbons as chemiresistors. *Adv Mater.* 2012;24: 53–57. doi:10.1002/adma.201102663
7. Yong Y, Dong X, Chan-Park M, Song H, Chen P. Macroporous and monolithic anode based on polyaniline hybridized three-dimensional graphene for high-performance microbial fuel cells. *ACS Nano.* 2012; 2394–2400. Available: <http://pubs.acs.org/doi/abs/10.1021/nn204656d>
8. Chen Z, Ren W, Gao L, Liu B, Pei S, Cheng H-M. Three-dimensional flexible and conductive interconnected graphene networks grown by chemical vapour deposition. *Nat Mater.* Nature Publishing Group; 2011;10: 424–8. doi:10.1038/nmat3001
9. Li N, Zhang Q, Gao S, Song Q, Huang R, Wang L, et al. Three-dimensional graphene foam as a biocompatible and conductive scaffold for neural stem cells. *Sci Rep.* 2013;3: 1604. doi:10.1038/srep01604

CHAPTER FIVE: CONCLUSION

5.1 Summary and Discussion

In summary, in this effort, an open-source CVD has been designed, sourced, built, and programmed. This system is capable of both atmospheric pressure and low pressure growths, temperatures up to 1100° C, and substrates up to ~1 inch in width. Additionally, with the detailed parameter and recipe logging, past growths can quickly be audited for possible issues or repeated, allowing for quick system troubleshooting and high process repeatability. With the resulting system, we have grown both graphene and graphene foam, both shown to be of high quality.

With this open-source design, the engineering cost for other researchers building their own CVDs for 2D material growth will be substantially reduced, allowing labs to begin synthesizing and studying 2D materials on a smaller budget than was previously possible. Because the design is divided by subsystem, modifications can easily be made to the design if customization is desired, and customization of the final system can be carried out without voiding a system warranty because parts are warrantied individually, rather than the system. Also, because the automation software has been programmed in LabView, and device drivers exist as individual subVIs, additional systems can easily be added to the controls program via the programming of additional hardware drivers and their integration into the controls programs.

5.2 Future Work

The CVD system built for this study has become a workhorse in the production of both graphene and graphene foam for numerous studies, including the use of both graphene and graphene foam as a substrate for cell growth and differentiation studies. Additionally, work is being conducted to synthesize high quality transition metal dichalcogenides, as described in the literature [1–3].

Possible future modifications of the CVD design include the addition of solid and liquid precursor injection ports for the injection of sulfur for transition metal disulfide growths, a cold finger on the exhaust side of the growth tube to condense low vapor pressure effluents, and the addition of a fourth gas line as needed by future experimental efforts. In the long term, a mass spectrometer or residual gas analyzer may be attached to the exhaust manifold in order to determine the identity and concentration of process exhaust gases. Additionally, a removable plasma generating attachment has been considered to enable plasma-enhanced CVD growths.

5.3 References

1. Lee YH, Zhang XQ, Zhang W, Chang MT, Lin C Te, Chang K Di, et al. Synthesis of large-area MoS₂ atomic layers with chemical vapor deposition. *Adv Mater.* 2012;24: 2320–2325. doi:10.1002/adma.201104798
2. Huang X, Zeng Z, Zhang H. Metal dichalcogenide nanosheets: preparation, properties and applications. *Chem Soc Rev.* 2013;42: 1934–46. doi:10.1039/c2cs35387c
3. Najmaei S, Liu Z, Zhou W, Zou X, Shi G, Lei S, et al. Vapour phase growth and grain boundary structure of molybdenum disulphide atomic layers. *Nat Mater.* Nature Publishing Group; 2013;12: 754–9. doi:10.1038/nmat3673

CHAPTER SIX: SUPPLEMENTARY INFORMATION

6.1 Supplementary Materials Folder Description

The following represents a file tree of the contents of 'Supplementary Materials.zip'. File and folder names are self-explanatory, but extra information has been provided in italics when deemed useful.

- Supplementary Materials
 - Programs
 - CVD Run Log – *Folder where ManualControls.vi and Read&RunRecipe.vi deposit run and recipe logs.*
 - Recipes
 - Quick.csv – *Example recipe. This is the same recipe used in the test case in Chapter Three.*
 - Sub-VIs – *Folder containing active component LabView drivers.*
 - Arduino Code.txt – *Code for the use of an Arduino in place of an analog input module in the cDAQ.*
 - Excel CVD Graphing Macro.txt – *Text of the Excel graphing macro for log files. Must be pasted into Excel's macro programming interface.*
 - ManualControls.vi – *Manual control program, as described in Chapter Three.*
 - Read&RunRecipe.vi – *Automated control program, as described in Chapter Three.*
 - Support Drawings – *Folder containing reference drawings for support structures. Dimensions of structures should be verified against user's specific system requirements prior to manufacture.*
 - Exhaust Line Support.pdf
 - Exhaust Manifold Support.pdf
 - Intake Manifold Support.pdf

- Large Support Base.pdf
- MFC Support.pdf – *Same general design concept used for valve supports in gas filter line and gas mixing line subsystems.*
- Construction Notes.pdf – *Detailed instructions on the construction of the described CVD system.*
- Parts List.xls – *List of parts with vendor and approximate price information for the CVD system described. Also contains options for user to change the number of gas lines and projected system price will update.*